Article

SOURCE DATA TRANSPARENT PROCESS

THE EMBO JOURNAL

# Proteolytic activation of angiomotin by DDI2 promotes angiogenesis

Yu Wang[1,†], Yuwen Zhu[1,†], Yebin Wang[1], Yue Chang[2,3], Fang Geng[2,3], Mingyue Ma[1], Yuan Gu[1], Aijuan Yu[1], Rui Zhu[1], Pengcheng Yu[1], Zhao Sha[1], Sixian Qi[1], Jian Li[1], Wencao Zhao[1,4], Weijun Pan[4], Ruilin Zhang[3,*] & Fa-Xing Yu[1,**]

## Abstract

**The scaffolding protein angiomotin (AMOT) is indispensable for vertebrate embryonic angiogenesis. Here, we report that AMOT undergoes cleavage in the presence of lysophosphatidic acid (LPA), a lipid growth factor also involved in angiogenesis. AMOT cleavage is mediated by aspartic protease DNA damage-inducible 1 homolog 2 (DDI2), and the process is tightly regulated by a signaling axis including neurofibromin 2 (NF2), tankyrase 1/2 (TNKS1/2), and RING finger protein 146 (RNF146), which induce AMOT membrane localization, poly ADP ribosylation, and ubiquitination, respectively. In both zebrafish and mice, the genetic inactivation of AMOT cleavage regulators leads to defective angiogenesis, and the phenotype is rescued by the overexpression of AMOT-CT, a C-terminal AMOT cleavage product. In either physiological or pathological angiogenesis, AMOT-CT is required for vascular expansion, whereas uncleavable AMOT represses this process. Thus, our work uncovers a signaling pathway that regulates angiogenesis by modulating a cleavage-dependent activation of AMOT.**

**Keywords** AMOT; angiogenesis; DDI2; NF2; protease
**Subject Categories** Development; Post-translational Modifications & Proteolysis; Vascular Biology & Angiogenesis
**DOI** 10.15252/embj.2022112900 | Received 24 October 2022 | Revised 23 May 2023 | Accepted 6 June 2023 | Published online 23 June 2023
**The EMBO Journal (2023) 42: e112900**

## Introduction

Blood vessels are crucial in the transport of fluids, gases, macromolecules, and cells in vertebrates, and abnormal vascular development contributes to various diseases, such as ischemia, blindness, and cancer (Carmeliet, 2003; Adams & Alitalo, 2007). Angiogenesis is the generation of new blood vessels from pre-existing vasculature, and in this process, endothelial cells (ECs) are specialized into leading tip cells and following stalk cells, and migrate in a collective manner to expand vasculature (Rorth, 2012; Mayor & Etienne-Manneville, 2016). Multiple signals and signaling pathways, such as vascular endothelial growth factor (VEGF) and Notch, are involved in regulating angiogenesis (Adams & Alitalo, 2007; Potente & Carmeliet, 2017). However, how migration of ECs is initiated and regulated remains poorly understood.

Angiomotin (AMOT), Angiomotin like 1 (AMOTL1), Angiomotin like 2 (AMOTL2), and shorter splicing isoforms constitute the Motin family proteins (Motins; Fig 1A; Moleirinho *et al*, 2014). Motins play important roles in endothelial biology, including the regulation of cell migration, stabilization of tight junctions and cell polarity, and transmission of mechanical force between cells, thus contributing to the establishment and maintenance of vascular networks (Wells *et al*, 2006; Ernkvist *et al*, 2009; Zheng *et al*, 2009; Hultin *et al*, 2014; Moleirinho *et al*, 2014; Zhang *et al*, 2021). It has been reported that knockout (KO) of *Amot* in mice leads to dilated and disorganized vasculature in yolk sacs, brain, and somites (Shimono & Behringer, 2003; Aase *et al*, 2007), and endothelial-specific KO of *Amot* significantly inhibits postnatal retinal angiogenesis (Zhang *et al*, 2021). Moreover, depletion of *amot* in zebrafish causes dilated primordial midbrain and hindbrain channels, defective intersegmental vessel (ISV), and absence of dorsal longitudinal anastomotic vessel (DLAV; Aase *et al*, 2007). Together, these results indicate that AMOT is an important regulator of angiogenesis.

Lysophosphatidic acid (LPA) is a lipid growth factor and chemotactic signal that plays diverse roles in vascular development (Mills & Moolenaar, 2003; Sumida *et al*, 2010). Autotaxin (*Atx*, responsible for LPA synthesis) or LPA receptor 4 (*Lpar4*) KO in mice causes profound vascular defects during embryonic development (van Meeteren *et al*, 2006; Sumida *et al*, 2010), and knockdown of *atx* or LPA receptors (*lpar1/4*, major LPA receptors in endothelial cells) in

1 Institute of Pediatrics, Children's Hospital of Fudan University, and the Shanghai Key Laboratory of Medical Epigenetics, the International Co-laboratory of Medical Epigenetics and Metabolism, the State Key Laboratory of Genetic Engineering, Institutes of Biomedical Sciences, Shanghai Medical College, Fudan University, Shanghai, China
2 School of Life Sciences, Fudan University, Shanghai, China
3 TaiKang Medical School (School of Basic Medical Sciences), Hubei Provincial Key Laboratory of Developmentally Originated Disease, Wuhan University, Wuhan, China
4 Key Laboratory of Tissue Microenvironment and Tumor, CAS Center for Excellence in Molecular Cell Science, Shanghai Institute of Nutrition and Health, University of Chinese Academy of Sciences, Chinese Academy of Sciences (CAS), Shanghai, China
*Corresponding author. Tel: +86 27 68759795; E-mail: zhangruilin@whu.edu.cn
**Corresponding author. Tel: +86 21 54237834; E-mail: fxyu@fudan.edu.cn
†These authors contributed equally to this work

zebrafish also results in defective ISV and DLAV (Yukiura *et al*, 2011). These phenotypes produced by LPA signaling deficiency resemble that of *AMOT* KO (Shimono & Behringer, 2003; Aase *et al*, 2007). We and others have shown that LPA signaling can effectively dephosphorylate and destabilize AMOT (Dai *et al*, 2013; Adler *et al*, 2013b; Wang *et al*, 2021), suggesting that AMOT is negatively regulated by LPA. However, it is unclear why both AMOT protein and LPA signaling are similarly required for angiogenesis.

In this study, we report that AMOT undergoes cleavage in the presence of LPA signals, and the cleavage serves as a switch, turning AMOT from an inhibitory to a stimulatory factor in vascular development. We have also dissected a signaling pathway regulating AMOT cleavage and revealed its critical function in both physiological and pathological angiogenesis.

## Results

### AMOT undergoes proteolytic cleavage

It has been shown previously that AMOTp130 protein is regulated by ubiquitin proteasome system (UPS; Wang *et al*, 2012, 2015b,

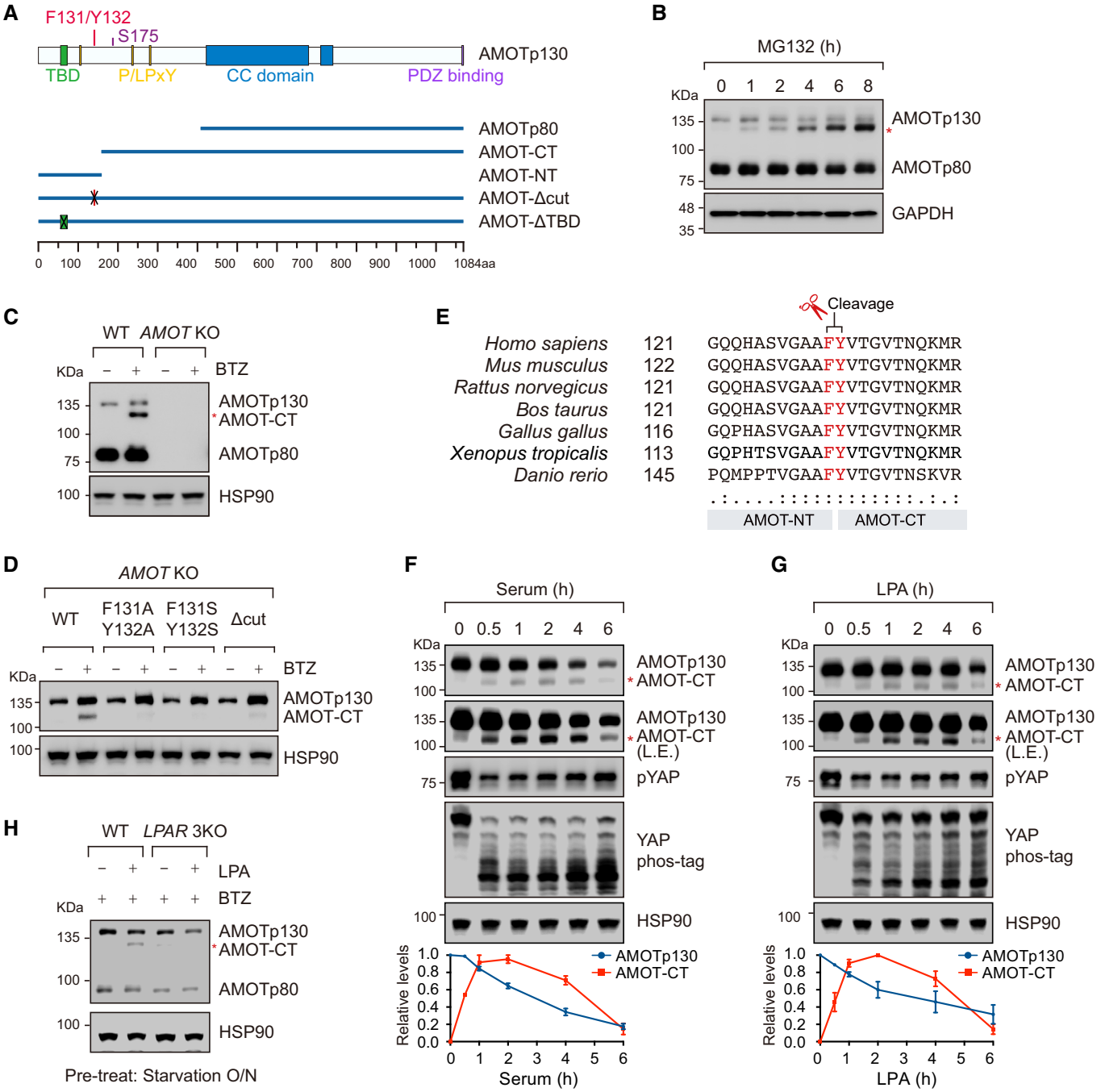


**Figure 1.**

**Figure 1. AMOT is cleaved into fragments undergoing rapid turnover.**

A The domain organization of AMOT proteins. AMOT gene encodes two isoforms sharing the same C-terminal sequence: AMOTp80 and AMOTp130. Unless otherwise indicated, we use AMOT for AMOTp130. The Coiled-coil (CC) domain and the extreme C-terminal PDZ-binding domain are present in both isoforms. AMOT has a unique N-terminal region containing LATS1/2 targeting site (S175), TNKS1/2-binding site (TBD), and three PPxY motifs. The position of F131/Y132 is also indicated.

B Proteasome inhibitor treatment (10 μM MG132 for 1 to 8 h) promotes accumulation of a ~110 KD fragment (asterisk) in HEK293A cells.

C The ~110 KD fragment (asterisk) is related to AMOT. Wild-type (WT) and *AMOT* knockout (KO) HEK293A cells were treated with 10 μM proteasome inhibitor bortezomib (BTZ) for 6 h and subjected to Western blotting analysis using the indicated antibodies.

D F131/Y132 is the cleavage site on AMOT. Wide-type (WT), F131/Y132 point mutant (F131A/Y132A, F131S/Y132S) and F131/Y132-deleted mutant (Δcut) AMOT were expressed in *AMOT* KO HEK293A cells. Cells were treated with 10 μM BTZ for 6 h.

E Protein sequence alignment shows that the AMOT cleavage site (F131/Y132) is highly conserved among different vertebrates.

F, G Serum and LPA treatments induce AMOT degradation and promote the accumulation of a ~110 kDa protein (asterisk) in HEK293A cells. Cells were serum-starved overnight and then treated with 10% FBS or 1 μM LPA for the indicated time. The phosphorylation levels of YAP proteins were detected by Phos-tag gel and pYAP immunoblotting. Protein quantification is shown below. Data represent mean ± SEM from three independent experiments. L.E. indicates long exposure.

H *LPAR1/2/3* knockout (LPAR 3KO) blocks the accumulation of ~110 kDa protein (asterisk). Cells were starved overnight and then treated with 10 μM BTZ and 1 μM LPA for 6 h, after which samples were harvested and subjected to Western blotting analysis using the indicated antibodies.

Source data are available online for this figure.

2016, 2021; Adler *et al*, 2013a; Campbell *et al*, 2016; Troilo *et al*, 2016). However, when cells were treated with the proteasome inhibitor MG132, AMOTp130 protein was not accumulated as expected. Rather, a smaller protein at ~110 kDa was gradually induced (asterisk, Fig 1B). The 110 kDa protein was also detected in cells treated with different proteasome inhibitors including bortezomib (BTZ; Fig EV1A). The 110 kDa protein was related to AMOT, as it was not detected in *AMOT* KO cells, regardless if BTZ was present (Fig 1C). Moreover, when an N-terminally FLAG-tagged AMOT was ectopically expressed in *AMOT* KO cells, not only the 110 kDa protein but also a ~20 kDa fragment was clearly detected upon BTZ treatment (Fig EV1B). We further observed that antibodies targeting the C-terminus or middle portion (amino acids 174–279), but not the N-terminus of AMOT, immunoprecipitated and recognized the 110 kDa protein (Fig EV1C and D). These results indicate that AMOT can be cleaved into a 110 kDa C-terminal fragment and a 20 kDa N-terminal fragment dubbed as AMOT-CT and AMOT-NT, respectively (Fig 1A). The cleavage product of AMOT might undergo rapid turnover, as it was not easily detected in the absence of proteasome inhibitors.

To identify the cleavage site in AMOT, we generated AMOT constructs with deletions of 50 or 10 amino acids. The sequences of amino acids 70–80 and 120–140 were essential for the generation of -AMOT-CT (Fig EV1E and F). Based on the molecular weight of AMOT-CT and AMOT-NT, we reasoned that the cleavage site in AMOT should be located within amino acids 120–140. In a refined analysis, AMOT with phenylalanine 131 (F131) and tyrosine 132 (Y132) deleted (AMOT-Δcut) or mutated were resistant to cleavage (Figs 1D and EV1G). In addition, a FLAG tag inserted before and after F131/Y132 was sorted, respectively, into AMOT-NT and AMOT-CT following BTZ treatment (Fig EV1H and I). We also found that AMOT PPxY motif mutations have no effect on cleavage (Fig EV1J). The amino acid sequences around F131/Y132 were highly conserved among different species (Fig 1E). The Motin family protein AMOT-like 1 (AMOTL1), but not AMOT-like 2 (AMOTL2), shared a similar cleavage sequence (Fig EV1K), and ectopically expressed AMOTL1 but not AMOTL2 could be cleaved (Fig EV1L and M). Together, these results indicate that AMOT is cleaved at F131/Y132 to generate AMOT-NT and AMOT-CT, and similar cleavage may also occur in AMOTL1.

### AMOT cleavage is induced by LPA signaling

Next, we asked whether the cleavage of AMOT is a regulated process. It has been shown previously that serum and LPA can regulate the protein stability of AMOT (Dai *et al*, 2013; Adler *et al*, 2013b; Wang *et al*, 2021). Indeed, in the presence of serum or LPA, AMOTp130 protein levels gradually decreased over time (Fig 1F and G). Interestingly, a similar accumulation of AMOT-CT was observed upon stimulation with LPA or serum; AMOT-CT level accumulated gradually to a peak within 2 h and then decreased (Fig 1F and G). Moreover, Sphingosine-1-phosphate (S1P), another bioactive lipid similar to LPA, also induced the production of AMOT-CT (Fig EV1N). On the other hand, several other proangiogenic factors present in serum, such as FGF2, VEGF, or heparin, failed to induce AMOT-CT (Fig EV1O and P), suggesting that AMOT cleavage is specifically regulated by LPA and S1P. LPA and S1P elicit intracellular signaling events by binding to their cognate G-protein-coupled receptors to induce cell proliferation and cell migration (Ishii *et al*, 2004). In cells with *LPAR1/2/3* (three major LPA receptors in HEK293A cells) deletion, LPA failed to induce AMOT-CT (Figs 1H and EV1Q), indicating an essential role of canonical LPA signaling in regulating AMOT cleavage. S1P may regulate AMOT cleavage via different S1P receptors, which is not explored further.

In the time course of serum or LPA treatment, AMOT-CT appeared after half an hour, gradually accumulated, and started to decline after 2 h (Fig 1F and G). These results indicate that the effect of serum and LPA on AMOT cleavage was rapid and also transient, and the newly formed AMOT-CT was subjected to degradation. Indeed, AMOT-CT was weakly detected upon proteasome inhibition without serum or LPA, or in the presence of LPA and serum alone without proteasome inhibition (Fig EV1R). On the other hand, AMOT-CT level was much higher when cells were treated with both proteasome inhibitor and LPA or serum (Fig EV1R). Hence, AMOT-CT generated in response to LPA signaling undergoes rapid turnover.

### Aspartic proteases DDI1/2 mediate AMOT cleavage

The human genome encodes more than 500 proteases that hydrolyze peptide bonds. These proteases fall into five major classes:

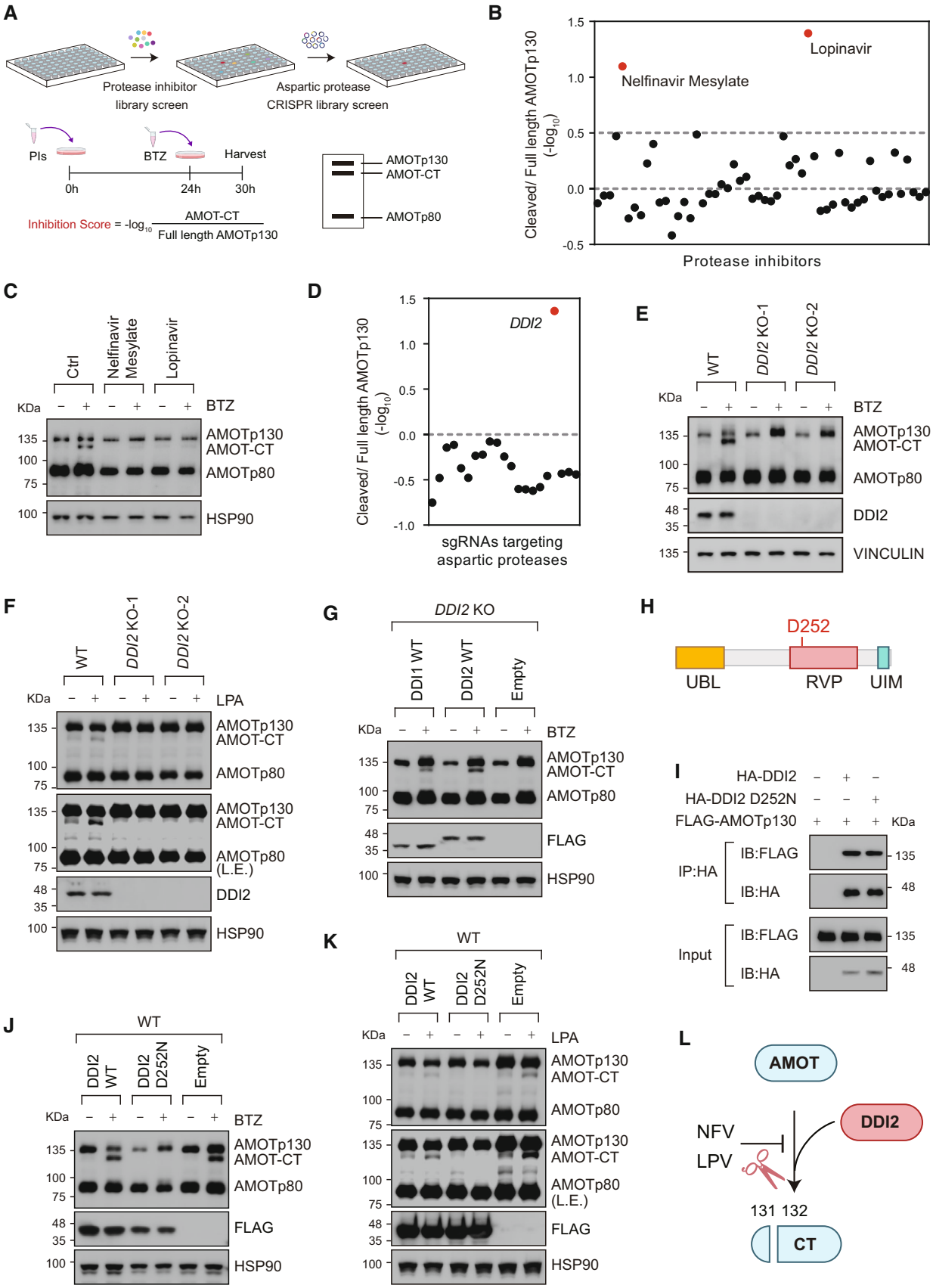


**Figure 2.**

**Figure 2. Aspartic proteases DDI1/2 mediate AMOT proteolysis.**

A Screening strategy for potential protease responsible for AMOT cleavage.
B, C Nelfinavir (NFV) and Lopinavir (LPV) block AMOT cleavage. HEK293A cells were pretreated with protease inhibitors overnight followed by 10 μM BTZ treatment for 6 h. Cell lysates were then subjected to Western blotting. See also Appendix Fig S1 and Table S1.
D, E Aspartic protease DDI2 is responsible for AMOT cleavage. Protease-related knockout HEK293A pools were treated with 10 μM BTZ for 6 h before harvest. See also Fig EV2 and Appendix Table S2.
F Deletion of *DDI2* blocks AMOT cleavage. Wild-type (WT) and *DDI2* KO cells were serum-starved overnight and then treated with 1 μM LPA for 2 h.
G Both DDI1 and DDI2 mediate AMOT cleavage. Ectopically expressed FLAG-tagged DDI1 or DDI2 rescues AMOT cleavage in *DDI2* KO HEK293A cells.
H Domain structures and motifs of DDI2. The active site aspartic acid 252 is shown.
I DDI2 interacts with AMOT. HEK293A cells were transfected with indicated plasmids, and FLAG-tagged AMOT was co-immunoprecipitated with wild-type DDI2 or protease-dead DDI2 (D252N) in HEK293A cell lysates.
J, K The aspartic catalytic-site mutant DDI2 exhibits a dominant negative effect through the inactivation of wild-type DDI2 in HEK293A cells. Wild-type HEK293A cells were transfected with the indicated plasmids and treated with BTZ for 6 h (J) or 1 μM LPA (K) before harvest.
L Schematic diagram of DDI2 working model.

Source data are available online for this figure.

aspartic, cysteine, metallo, serine, and threonine proteases (Puente *et al*, 2003). To search for the protease involved in AMOT cleavage, we screened a library of protease inhibitors that were capable of inhibiting different proteases. We identified two HIV protease inhibitors, Nelfinavir (NFV) and Lopinavir (LPV), which effectively blocked AMOT cleavage (Fig 2A–C, and Appendix Fig S1 and Table S1). HIV protease is an aspartic protease. Hence, an endogenous aspartic protease responsible for AMOT cleavage might be targeted by NFV and LPV. We then knocked out all human aspartic proteases one by one using the CRISPR/Cas9 approach (Puente *et al*, 2003; Appendix Table S2). Among all aspartic proteases, only depletion of *DDI2*, using two independent guide sequences, significantly blocked AMOT cleavage in the presence of BTZ or LPA (Figs 2D–F and EV2A). In *DDI2*-deficient cells, both DDI2 and its paralog DDI1 rescued the cleavage of AMOT, suggesting DDI1 and DDI2 worked equivalently (Fig 2G). However, DDI1 was not expressed in most somatic cells and was not targeted in the screen (Fig EV2A). We also observed that both wild-type DDI2 and an enzymatically dead DDI2 mutant (D252N) interacted with AMOT (Fig 2H and I), whereas the D252N mutant functioned in a dominant negative manner to block AMOT cleavage (Fig 2J and K). These data suggest that DDI2 is the protease responsible for AMOT cleavage and the generation of AMOT-CT (Fig 2L).

### A NF2-TNKS-RNF146 signaling axis regulates AMOT cleavage

To investigate the regulatory mechanism underlying DDI2-mediated AMOT cleavage, we first looked at AMOT ubiquitination since DDI2 has a ubiquitin-interacting motif (UIM) and ubiquitin-associated (UBA) domain important for interaction with ubiquitinated proteins (Fig 2H). MLN7243, a ubiquitin-activating enzyme (E1) inhibitor, completely blocked protein ubiquitination and AMOT cleavage, indicating that AMOT cleavage was a ubiquitination-dependent process (Fig 3A). To identify the E3 ligase involved in AMOT cleavage, we knocked out each reported E3 ligase for AMOT and found that only *RNF146*-KO fully blocked AMOT cleavage (Wang *et al*, 2012, 2015b; Mercenne *et al*, 2015; Figs 3B and EV2B). AMOT is poly ADP-ribosylated (PARylation) by TNKS1/2 and then ubiquitinated by RNF146, which is critical for AMOT protein stability (Wang *et al*, 2015b, 2016, 2021; Campbell *et al*, 2016; Troilo *et al*, 2016).

**Figure 3. LPA-stimulated PARylation and ubiquitination of AMOT are crucial for DDI2-mediated cleavage.**

A Ubiquitination is required for AMOT cleavage. HEK293A cells were treated with 100 nM E1 inhibitor MLN7243 overnight followed by 10 μM BTZ for 6 h. Cell lysates were then subjected to Western blotting.
B, C The TNKS1/2-RNF146 axis is crucial for AMOT cleavage. Wild-type (WT), *TNKS1/2* double KO (dKO), and *RNF146*-KO HEK293A cells were treated with the proteasome inhibitor MG132 for 6 h before harvest. Cell lysates were subjected to Western blotting analysis using the indicated antibodies.
D TNKS1/2 inhibition blocks AMOT cleavage. HEK293A cells were treated with 10 μM XAV939 (a TNKS1/2 inhibitor) or Olaparib (a PARP inhibitor) for 24 h followed by 10 μM BTZ for 6 h.
E TNKS1/2-binding is essential for AMOT cleavage. Deletion of the Tankyrase-binding domain (ΔTBD) in AMOT abolished AMOT cleavage. Exogenous wild-type AMOT or Tankyrase-binding domain deleted AMOT was transfected into *AMOT* KO cells and cells were treated with the proteasome inhibitor BTZ for 6 h before harvest.
F NF2 is essential for AMOT cleavage. Wild-type (WT) and *NF2*-KO HEK293A cells were treated with the proteasome inhibitor MG132 for 6 h before harvest.
G *NF2* deficiency blocks AMOT cleavage. Hippo pathway component knockout (KO) cell lines and control HEK293A cells were treated with or without 10 μM BTZ for 6 h. AMOT-CT/AMOT ratios were quantified by calculating their band signals. MM9 indicates *MAP4K1–7* and *MST1/2* 9KO. The results were shown as the mean ± SEM of three biological replicates.
H, I AMOT cleavage states in different cell lines with *NF2*-wild-type or *NF2* deficiency.
J TNKS inhibition blocks serum-induced AMOT cleavage. HEK293A cells were serum-starved overnight in the presence or absence of 10 μM XAV939 and then treated with 10% FBS for 2 h.
K Serum, LPA, and S1P stimulate PARylation and ubiquitination of AMOT. Serum-starved cells were treated with 10% FBS, 1 μM LPA, or 1 μM S1P for 4 h and subjected to an immunoprecipitation (IP) assay.
L Schematic diagram of the AMOT proteolytic pathway. LPARs, class A GPCRs, transduce a lysophosphatidic acid (LPA) signal across the cell membrane and activate NF2. NF2 facilitates the recruitment of TNKS1/2 and RNF146 to promote PARylation and ubiquitination of AMOT. DDI2 recognizes the specific ubiquitination modification of AMOT and promotes its proteolysis.

Source data are available online for this figure.

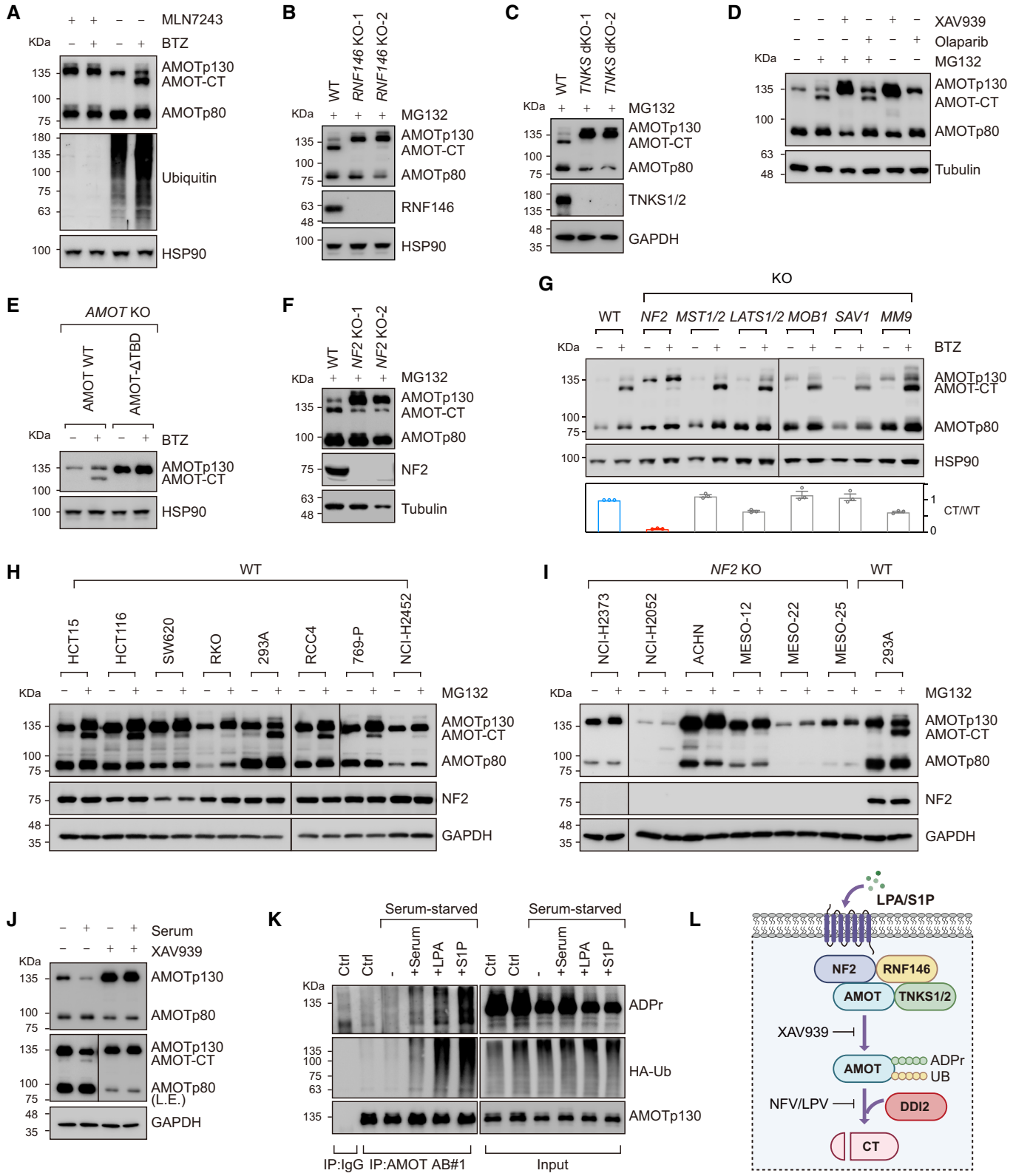


**Figure 3.**

We found that *TNKS1/2* KO or tankyrase inhibitor (XAV939) treatment effectively blocked AMOT cleavage (Figs 3C and D, and EV2C and D). Moreover, an AMOT mutant lacking tankyrase-binding domain (AMOT-ΔTBD, amino acids 77–84 deleted) could not be cleaved, and mutational analysis showed this region to be critical for AMOT cleavage (Figs 3E, and EV1E and F). AMOT-ΔTBD is

 

unable to undergo PARylation and subsequent ubiquitination (Wang *et al*, 2015b). We found that, compared with wild-type AMOTp130, the interaction between AMOT-ΔTBD and DDI2 was much weaker, indicating that the interaction was dependent on ubiquitination (Fig EV2E). In *DDI2* KO cells, the protein level of AMOTp130 was not dramatically increased as that in *TNKS1/2* or *RNF146*-KO cells, indicating that AMOT cleavage by DDI2 was not required for AMOTp130 degradation (Fig EV2F). Together, these results demonstrate that the cleavage of AMOT by DDI2 is a process dependent on PARylation and ubiquitination catalyzed by TNKS1/2 and RNF146, respectively. However, the cleavage and degradation of AMOTp130 are not coupled, as DDI2 is not required for AMOTp130 degradation.

Our previous work has shown that NF2 promotes junctional localization of AMOT, RNF146, and TNKS1/2 upon serum or LPA stimulation, and this process is required to induce the ubiquitination and degradation of AMOT (Wang *et al*, 2021). We found that AMOT-CT was largely absent in *NF2*-deficient cells, indicating a critical role of NF2 in AMOT cleavage (Fig 3F). NF2 is a key component of the Hippo signaling pathway and is frequently mutated in human cancers (Benhamouche *et al*, 2010; Zhang *et al*, 2010; Zanconato *et al*, 2016). To test whether additional Hippo pathway components, such as MST1/2, LATS1/2, MOB1A/B, SAV1, and MAP4K kinases, were involved in the regulation of AMOT cleavage, different KO cells were established and their responses to BTZ were analyzed. However, deficiency of Hippo pathway genes other than *NF2* failed to effectively block the production of AMOT-CT (Fig 3G). We also collected cancer cell lines with or without *NF2* mutation and observed that the accumulation of AMOT-CT upon BTZ treatment occurred only in cells with wild-type *NF2* (Fig 3H and I). These results suggest that NF2 is required for AMOT cleavage, and this function is not shared by other Hippo pathway components. In *RNF146*, *TNKS1/2* and *NF2*-KO cells, or in the presence of tankyrase inhibitor XAV939, LPA- or serum-induced AMOT cleavage was also largely abolished (Figs 3J and EV2G–I). Moreover, the PARylation and ubiquitination of AMOT were induced upon serum or LPA stimulation (Fig 3K). Together, these results suggest that NF2, regulated by LPA signaling and its cognate receptors, recruits AMOT, TNKS1/2, and RNF146 to promote PARylation and ubiquitination of AMOT, which in turn leads to enhanced AMOT cleavage by DDI2 (Fig 3L).

### The proteolysis pathway of AMOT is highly conserved in endothelial cells

Angiomotin has been shown to stimulate endothelial cell motility and is required for angiogenesis (Aase *et al*, 2007; Zhang *et al*, 2021). To explore the function of AMOT cleavage in angiogenesis, we first determine whether this cleavage pathway is conserved in endothelial cells. Similar to HEK293A cells, AMOT, and upstream regulatory proteins involved in AMOT cleavage were all expressed in HUVEC and primary endothelial cells isolated from mouse kidney, brain, and liver, and proteasome inhibitor treatment also led to the accumulation of AMOT-CT (Fig 4A and B, and Appendix Fig S2A and B). Knockdown of *DDI2* by siRNA or inhibition of DDI2 by NFV or LPV significantly blocked AMOT cleavage in HUVEC cells (Fig 4C and D). Moreover, tankyrase inhibitor (XAV939) treatment, and *RNF146* or *NF2* knockdown also effectively blocked AMOT cleavage (Fig 4E–G). To further examine the function of AMOT cleavage in angiogenesis, we performed a transwell assay using HUVEC and HMEC1 cells expressing full-length AMOT, uncleavable AMOT (Δcut), or AMOT-CT, and the results indicated that only AMOT-CT significantly promoted endothelial cell migration (Appendix Fig S2C–F). Furthermore, we also performed a spheroid-based sprouting assay using HUVEC cells to study angiogenesis in a 3D environment (Tetzlaff & Fischer, 2018). Interestingly, a significant increase in sprouting length and tip cell number was observed when AMOT-CT but not the other forms of AMOT were expressed (Fig 4H–J). Together, these data indicate that the AMOT cleavage pathway is conserved in endothelial cells, and AMOT-CT induces angiogenesis *in vitro*.

### The AMOT cleavage pathway is crucial for zebrafish embryonic vascular development

To further understand the physiological role of AMOT cleavage in angiogenesis, we assessed the effect of Amot cleavage on ISV and DLAV formation, in a well-established angiogenesis model in zebrafish embryonic development (Aase *et al*, 2007). As reported, Morpholinos (MO) targeting *amot* and LPA receptors (*lpar1/4*) blocked dorsal migration of endothelial cells and the formation of ISV and DLAV (Fig 5A–D and Appendix Fig S3A and B; Aase

**Figure 4. The AMOT cleavage pathway is conserved in endothelial cells.**

A The AMOT cleavage pathway is conserved in HUVECs. Red asterisk indicates AMOT-CT.

B Proteasome inhibitor treatment (10 μM BTZ for 1 to 8 h) promotes the accumulation of AMOT-CT in HUVEC cells.

C Nelfinavir and Lopinavir block AMOT cleavage in HUVECs. HUVECs were pretreated with protease inhibitors overnight followed by 10 μM BTZ treatment for 6 h. Cell lysates were subjected to Western blotting. Protein quantification is shown below.

D Aspartic protease DDI2 is responsible for AMOT cleavage in HUVECs. HUVECs were transfected with two different small interfering RNA (siRNA), and 48 h post-transfection, the cells were treated with 10 μM BTZ for 6 h. Cell lysates were subjected to Western blotting. Protein quantification is shown below.

E TNKS1/2 inhibitor XAV939 blocks AMOT cleavage. HUVECs were treated with 10 μM XAV939 for 24 h followed by 10 μM BTZ for 6 h.

F, G RNF146 and NF2 are indispensable for AMOT cleavage in HUVECs. siRNAs were transfected into HUVECs, the cells were treated with 10 μM BTZ for 6 h before harvest. Protein quantifications are shown below.

H Representative immunofluorescence images of HUVEC spheroids 18 h after VEGF stimulation. Above: inverted contrast images. Areas within the red dash box indicate the region of interest (ROI) and are shown below at higher magnification. Plasma membranes were stained with CellMask (red), actin filaments with Phalloidin (green), and nucleus with DAPI (blue). Scale bar 100 μm. HUVECs infected with empty vector virus were used as control.

I, J Quantification of the number of sprouts per spheroid and the cumulative sprout length of HUVECs. Vector ($n$ = 20), AMOT-WT ($n$ = 18), AMOT-ΔTBD ($n$ = 14), AMOT-Δcut ($n$ = 15), AMOTp80 ($n$ = 16), AMOT-NT ($n$ = 17), and AMOT-CT ($n$ = 21).

Data information: Data are shown as mean ± SEM from at least three biological replicates. Statistical significance was determined using the Student's $t$-test, *$P < 0.05$, **$P < 0.01$, ***$P < 0.001$, n.s. indicates not significant.
Source data are available online for this figure.

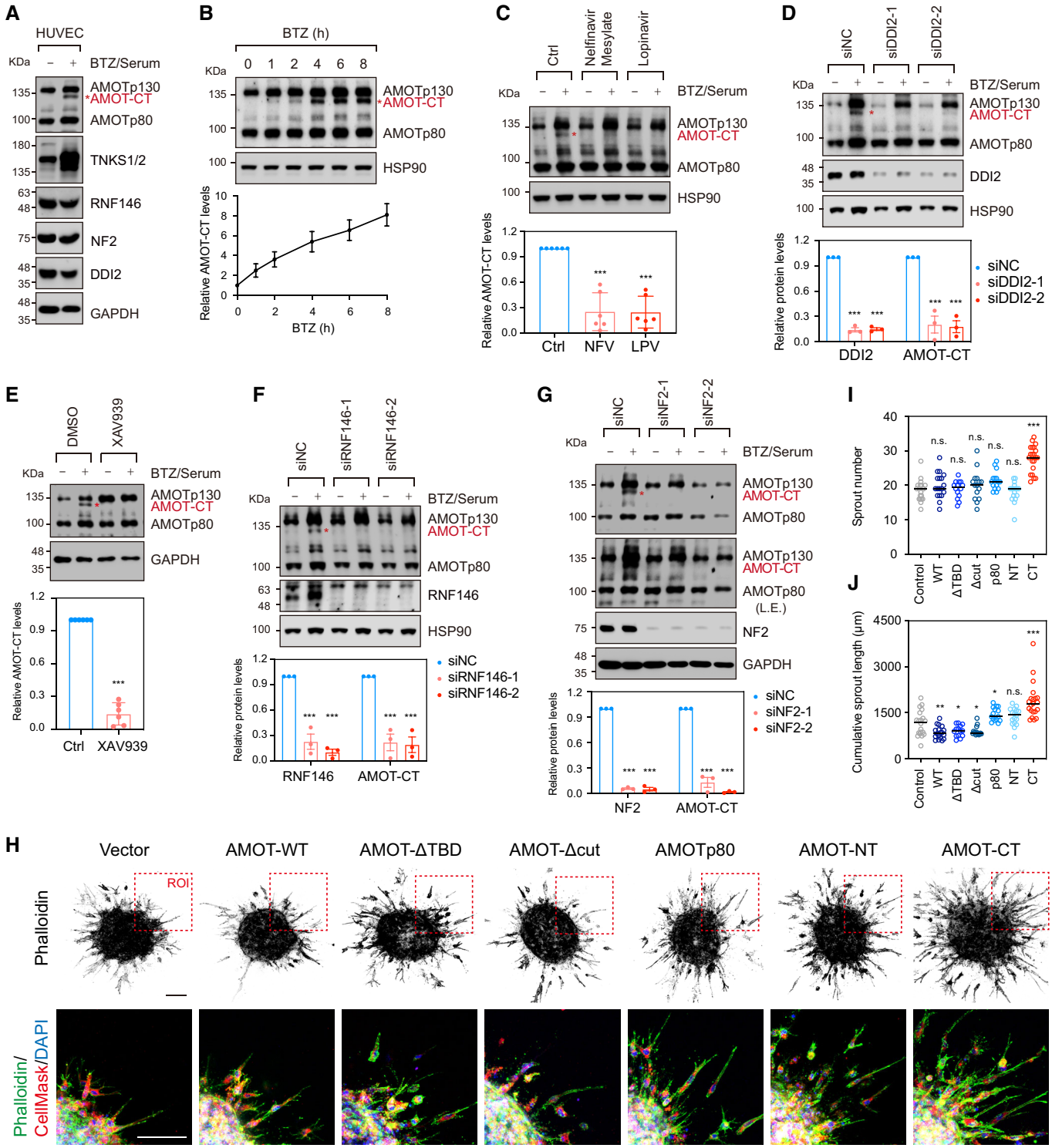


**Figure 4.**

*et al*, 2007; Yukiura *et al*, 2011). Interestingly, the knockdown of *tnks1/2*, *rnf146*, or *ddi2* resulted in a similar phenotype, suggesting that these proteins may work in a cascade to regulate ISV formation by controlling AMOT cleavage (Fig 5C and D, and Appendix Fig S3B). In *amot* knockdown embryos, put-back of RNA corresponding to human AMOT or AMOT-CT, but not AMOT-NT, AMOT-Δcut, or AMOT-ΔTBD mutants (the latter two mutants could not be cleaved), rescued the ISV defect, indicating that the generation of AMOT-CT is essential for AMOT function in angiogenesis (Fig 5E and F, and Appendix Fig S3C). In support of this notion, in *ddi2*-deficient embryos, put-back of AMOT-CT, but not full-length AMOT, rescued ISV development (Fig 5G and H, and Appendix

 

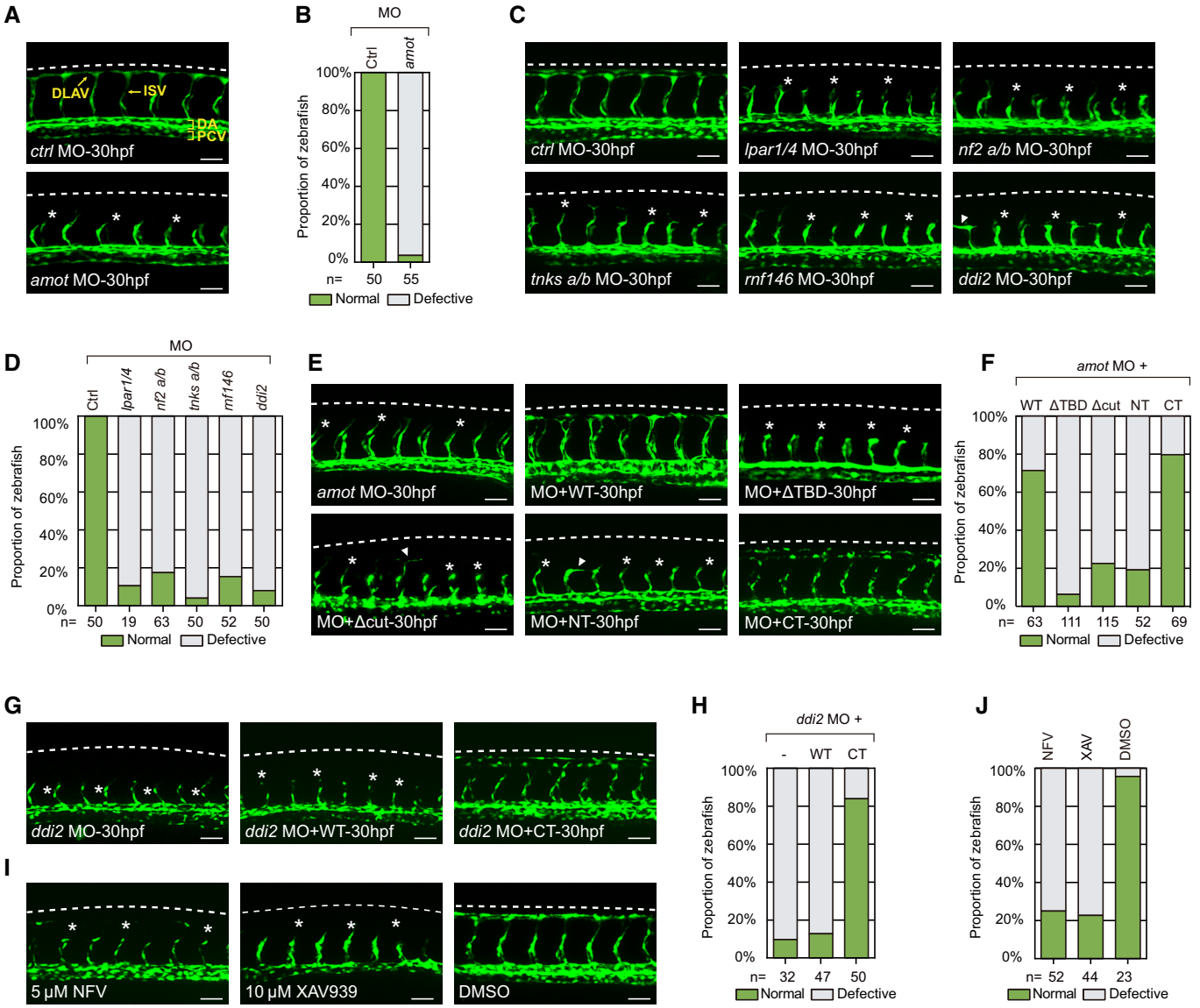


**Figure 5. The cleavage of AMOT is indispensable for embryonic angiogenesis in zebrafish.**

A, B Knockdown of *AMOT* induces vascular development defects in zebrafish embryos. Lateral views of ISV and DLAV formation in Tg*(flk:GFP)* control and *amot*-MO-injected zebrafish embryos at 30 h postfertilization (hpf) are shown. Histogram depicts the quantification of normal and angiogenesis-defective embryos at 30 hpf (B). *n*: number of embryos analyzed. Dorsolateral anastomose vessels (DLAV), intersegmental vessels (ISV), dorsal aorta (DA), and posterior cardinal vein (PCV) are shown. Asterisks: defective ISV; dotted lines: dorsal edge of the embryo. Scale bar: 50 μm.

C, D The entire pathway regulating AMOT proteolysis is required for zebrafish angiogenesis. Lateral views of the trunk regions of Tg*(flk:GFP)* zebrafish embryos injected with control and indicated MOs at 30 hpf are shown. Quantification of normal and angiogenesis-defective embryos is shown in (D). Asterisks: defective ISV; arrowheads: aberrant migration; dotted lines: dorsal edge of the embryo. *n*: number of embryos analyzed. Scale bar: 50 μm. Similar quantifications and annotations were used in (E–J).

E, F Noncleavable AMOT mutant fails to support angiogenesis. Embryos were injected with *amot*-MO together with mRNA encoding wild-type (WT) or mutant (ΔTBD, NT, CT, and Δcut) *AMOT*. Scale bar: 50 μm.

G, H AMOT-CT but not full-length AMOT could rescue impaired angiogenesis in *ddi2*-deficient embryos. Embryos were injected with *ddi2*-MO together with mRNA encoding wild-type *AMOT* (*AMOT-WT*) or *AMOT-CT*. Scale bar: 50 μm.

I, J Nelfinavir (NFV) and XAV939 repress ISV development. Embryos were treated with 5 μM NFV and 10 μM XAV939 at 6 hpf for 24 h. Number of ISV defects was counted at 30 hpf. Scale bar: 50 μm.

Source data are available online for this figure.

Fig S3D). Moreover, zebrafish embryos treated with NFV (Ddi2 inhibitor) or XAV939 (Tnks1/2 inhibitor) showed significant defects in ISV development while other organs and tissues were largely normal (Fig 5I and J, and Appendix Fig S3E). Hence, cleavage of Amot by Ddi2 is essential for its function in promoting zebrafish angiogenesis.

### AMOT cleavage is required for mouse retinal angiogenesis

The mouse retina is a well-established model for studying angiogenesis. Retinal angiogenesis in mice begins at postnatal day 0 (P0), and during the first week, hyaloid vessels rapidly regress and new vascular plexus forms through EC proliferation, sprouting, and migration, with the superficial endothelial network extending from the optic stalk to the retina edges at approximately P8. From P7 onward, superficial capillaries sprout vertically to form a second, deep vascular plexus, followed by the third, intermediate layer (Fig EV3A; Pitulescu *et al*, 2010; Stahl *et al*, 2010). We harvested retinas from mice at different angiogenic stages and subjected these samples to immunoblotting. Interestingly, AMOT-CT was detected in P4 and P6, but not in P18 retinas (Fig EV3B and C). Hence, the cleavage of AMOT and generation of AMOT-CT appeared to be associated with angiogenesis, and the process was turned off at the end of the angiogenic program. To test the effect of AMOT cleavage on retinal angiogenesis, we constructed conditional *AMOT-Δcut* and *AMOT-CT* transgenic mice and crossed with *Cdh5-Cre*ERT2 mice to express these genes specifically in ECs following tamoxifen injection (Figs 6A and EV3D, and Appendix Figs S4A–D and S5A–D). These two mouse lines were dubbed as $\Delta cut^{iEC\text{-}TG}$ and $CT^{iEC\text{-}TG}$, respectively, and the expression of corresponding proteins in ECs was confirmed by mNeonGreen staining (Appendix Figs S4E and S5E).

We first characterized retinal angiogenesis in $\Delta cut^{iEC\text{-}TG}$ mice. P6 retinas showed a significant decrease in vascular area, indicating compromised angiogenesis (Fig 6B and C). The vascular fronts of $\Delta cut^{iEC\text{-}TG}$ retinas were hyper-pruned, as indicated by fewer and shorter sprouts (Fig 6D). Some tip cells of $\Delta cut^{iEC\text{-}TG}$ retinas exhibited a blunted end (white arrow) instead of apiculiform-like morphology in control retinas (Fig 6D). The vascular network of $\Delta cut^{iEC\text{-}TG}$ retinas was less complex than that of control retinas, as shown by reduced branch points and sparse nuclei (Fig 6E and F). Moreover, tip cells in $\Delta cut^{iEC\text{-}TG}$ retinas had fewer filopodia, and quantitative analysis revealed a significant decrease in both filopodia density and length (Fig 6G and H).

AMOT-CT induced sprouting of endothelial cells (Fig 4H–J), hence we expected to see a stimulation of retinal angiogenesis upon transgenic expression of AMOT-CT. However, the vascular development in P6 $CT^{iEC\text{-}TG}$ retinas was similar to control retinas, as indicated by normal vascular area, length and numbers of sprouts, nuclei density, branch points, and filopodia density and length (Fig EV3E–J). It is possible that AMOT-CT generated during development is sufficient for retinal angiogenesis, hence ectopically expressed AMOT-CT may not lead to a proportional increase in angiogenesis.

To further investigate the inhibitory effect of uncleavable AMOT on angiogenesis, we generated an *AMOT-Δcut* knockin (*Δcut* KI) mice with amino acids F132 and Y133 of mouse AMOTp130 (corresponding to F131 and Y132 of human AMOTp130) deleted (Fig 6I and Appendix Fig S6). AMOT cleavage and CT generation were impaired in both isolated endothelial cells and whole retina from *Δcut* KI mice (Fig EV4A–C). We observed that *Δcut* KI retinas exhibited a decrease in vascular area, indicating compromised angiogenesis (Fig 6J and K). At the vascular front of *Δcut* KI retinas, although branch and sprout numbers were not significantly changed, the sprout length was shorter, and nuclei density was increased (Fig 6L and M). The overall phenotype of *Δcut* KI retinas was weaker than $\Delta cut^{iEC\text{-}TG}$ retinas. However, compared with controls, the specialized endothelial tip cells in *Δcut* KI retinas had shorter and fewer filopodia (Fig 6N and O). Together, these results suggest that the expression of uncleavable AMOT results in defective EC migration,

**Figure 6. AMOT cleavage is required for mouse retinal angiogenesis.**

A Left, schematic diagram of generation of endothelial-specific *AMOT-Δcut* overexpression ($\Delta cut^{iEC\text{-}TG}$) mice. Right, experimental strategy to assess retinal vascularization at P6. Mice were treated with tamoxifen at P3,4,5 and analyzed at P6.

B, C $\Delta cut^{iEC\text{-}TG}$ mice show the reduced retinal vascular area at P6. IB4 staining of the whole retina (B). Quantification of the vascular area of control and $\Delta cut^{iEC\text{-}TG}$ P6 retinas (C). Scale bar: 500 μm. Each dot represents one retina, control ($n$ = 12), and $\Delta cut^{iEC\text{-}TG}$ ($n$ = 14).

D $\Delta cut^{iEC\text{-}TG}$ mice have angiogenesis defects in the whole retina. Immunofluorescent images of P6 whole-mount retinas stained for IB4 (marker of blood vessels) and the endothelial factor ERG (marker of endothelial cell nuclei). Areas within white dash rectangles indicate the regions of interest (ROI), the sprouting front and vascular plexus between an artery and a vein are shown below at higher magnification. Arrowheads: blunt-ended tip ECs. Scale bar: 100 μm.

E Schematic diagram of the quantification method of sprout number, sprout length, and nuclei number at the sprouting front of the retina.

F Quantification of the number of branch points per $10^4$ $\mu m^2$, the number of sprouts per 100 μm sprouting front border (endothelial vessel length in panel E), the average length of sprouts, and the number of nuclei per 100 μm sprouting front border in control and $\Delta cut^{iEC\text{-}TG}$ P6 retinas. Each data point represents the average of two or three measurements from one retina, control ($n$ = 8), and $\Delta cut^{iEC\text{-}TG}$ ($n$ = 7).

G High magnification confocal images of filopodia extension at the leading edge of the retinal vascular in control and $\Delta cut^{iEC\text{-}TG}$ mice. Scale bar: 10 μm.

H Quantification of the number and average length of filopodia in control and $\Delta cut^{iEC\text{-}TG}$ P6 retinal sprouts. Each data point represents the average of three measurements from one retina, control ($n$ = 7), and $\Delta cut^{iEC\text{-}TG}$ ($n$ = 7).

I Experimental strategy to assess retinal vascularization. Control and *Δcut* KI mice were analyzed at P7.

J, K *Δcut* KI mice show the reduced retinal vascular area at P7. IB4 staining of the whole retina (J). Quantification of the vascular area of control and *Δcut* KI P7 retinas (K). Scale bar: 500 μm. Each dot represents one retina, control ($n$ = 24), and *Δcut* KI ($n$ = 18).

L *Δcut* KI mouse retinal angiogenesis shows sprouting defects in the sprouting front border. Immunofluorescent images of P7 whole-mount retinas stained for IB4 and ERG. White dash rectangles indicate regions of interest (ROI) are shown below. Arrowheads: blunt-ended tip ECs. Scale bar: 100 μm.

M Quantification of the retinal vasculature of control and *Δcut* KI mice at P7. Each data point represents the average of two or three measurements from one retina, control ($n$ = 8), and *Δcut* KI ($n$ = 8).

N High magnification confocal images of filopodia extension at the leading edge of the retinal vascular in control and *Δcut* KI mice. Tip cells are labeled with IB4. Scale bar: 10 μm.

O Quantification of the number and average length of filopodia in control and *Δcut* KI P7 retinal sprouts. Each data point represents the average of three measurements from one retina, control ($n$ = 8), and *Δcut* KI ($n$ = 8).

Data information: Data are shown as mean ± SEM from at least three independent littermates. Statistical significance was determined using the Student's $t$-test, $^*P < 0.05$, $^{**}P < 0.01$, $^{***}P < 0.001$, n.s. indicates not significant.
Source data are available online for this figure.

 

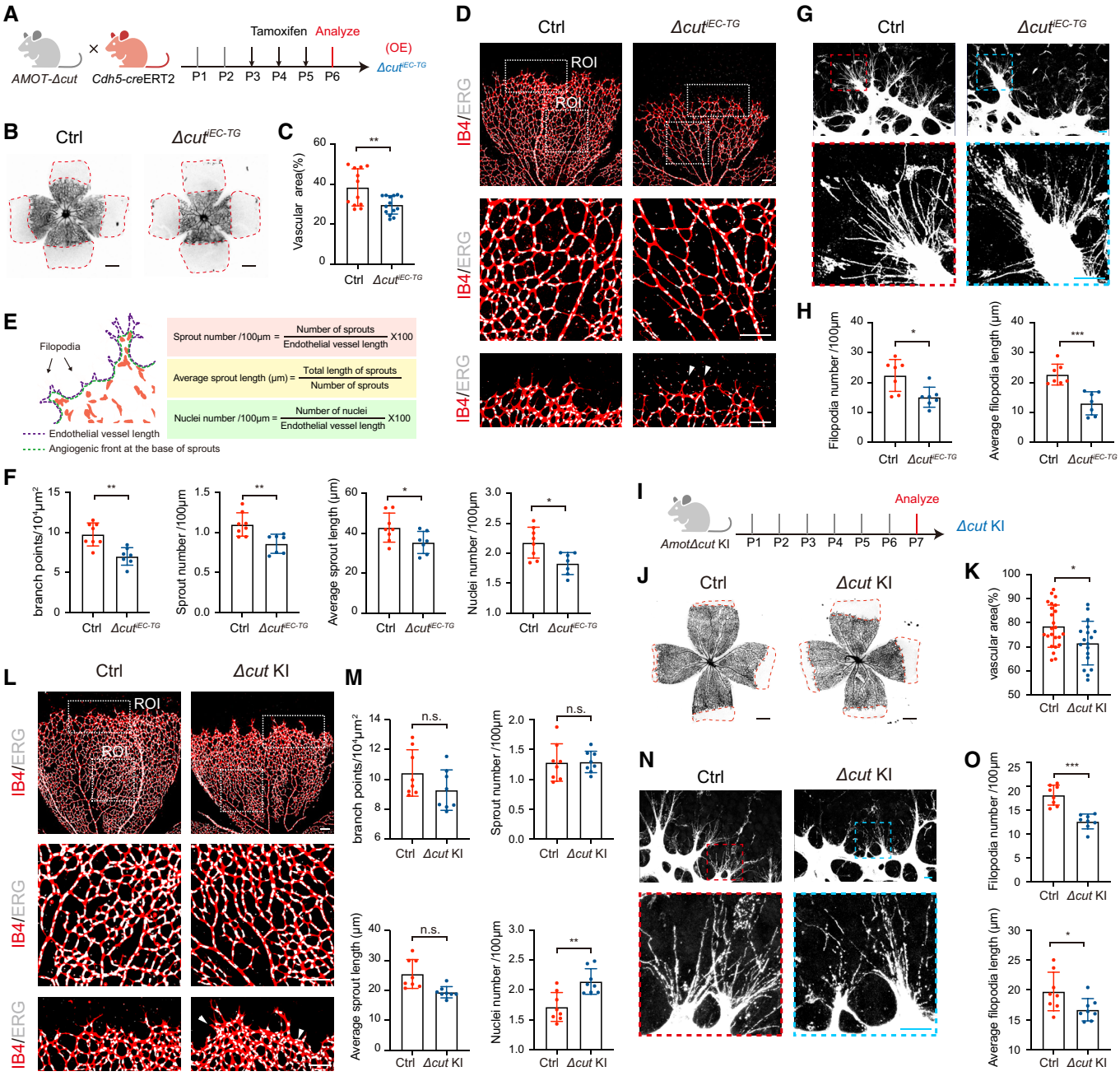


**Figure 4.**

impaired vascular network formation, and delayed retinal angiogenesis. These findings are surprising because AMOT has been shown previously indispensable for angiogenesis (Zhang *et al*, 2021).

AMOT family proteins, as upstream components of the Hippo pathway, bind directly to and inhibit YAP/TAZ activity (Chan *et al*, 2011; Paramasivam *et al*, 2011; Wang *et al*, 2011; Zhao *et al*, 2011). The interaction is mediated by PPxY motifs in AMOT proteins and WW domains in YAP/TAZ (Chan *et al*, 2011; Paramasivam *et al*, 2011; Wang *et al*, 2011; Zhao *et al*, 2011), and the first N-terminal PPxY motif is absent in AMOT-CT (Fig 1A). Previous studies have shown that the activity of YAP/TAZ is crucial for EC migration, proliferation, and filopodia formation, which are essential for vascular remodeling during retinal angiogenesis (Kim *et al*, 2017; Sakabe *et al*, 2017; Wang *et al*, 2017; He *et al*, 2018). Hence, the distinct effects of full-length AMOT and AMOT-CT on retinal angiogenesis might be caused by differences in YAP/TAZ activity. However, YAP target gene expression was decreased in both full-length AMOT- and AMOT-CT-overexpressing cells (Appendix Fig S7A). Moreover, different AMOT mutants, including AMOT-CT and AMOT-Δcut, inhibited cell proliferation as efficiently as AMOTp130 did *in vitro* (Appendix Fig S7B–E). In addition, the proliferation rate of retinal endothelial cells in *Δcut*$^{iEC\text{-}TG}$ and *CT*$^{iEC\text{-}TG}$ retinas was similar and comparable to that of control retinas (Appendix Fig S8). Thus, the inhibition of retinal angiogenesis by

uncleavable AMOT is unlikely due to YAP/TAZ activity and cell proliferation.

### DDI2-mediated AMOT cleavage is required for vascular development in the retina

To further investigate the role of AMOT cleavage in retinal angiogenesis, we tested whether DDI2, the enzyme responsible for AMOT cleavage, was required for retinal angiogenesis. We constructed *Ddi2*$^{fl/fl}$ mice, and generated EC-specific *Ddi2* deletion (*Ddi2*$^{iEC\text{-}KO}$; Fig 7A and Appendix Fig S9). Compared with controls, P6 *Ddi2*$^{iEC\text{-}KO}$ retinas presented compromised vessel growth as indicated by a reduction in vascular area (Fig 7B and C). The vascular front displayed impaired vessel sprouting, as indicated by fewer and shorter sprouts (Figs 7D and E, and EV4D). The branch points and nuclei density were also decreased in both angiogenic front and vessel plexus of *Ddi2*$^{iEC\text{-}KO}$ retinas (Fig 7D and E). Moreover, tip cells in the *Ddi2*$^{iEC\text{-}KO}$ mice had only a few filopodia extending from vessel termini (Fig 7F and G). The defect of retinal vasculature in Ddi2$^{iEC\text{-}KO}$ mice was identical to that of *Δcut*$^{iEC\text{-}TG}$ retinas (Fig 6D–F). The proliferation and migration of vascular endothelial cells are crucial for angiogenesis. Interestingly, deletion of *Ddi2* did not affect the number of proliferating endothelial cells (Fig 7H and I), implying that the defective angiogenesis in *Ddi2*$^{iEC\text{-}KO}$ retinas is likely caused by the impaired cell migration. Interestingly, AMOT-CT expression (*Ddi2*$^{iEC\text{-}KO}$; *CT*$^{iEC\text{-}TG}$) completely rescued the abnormalities in retinal vascular development, EC migration, and filopodia morphology caused by *Ddi2* deficiency (Fig 7). Hence, DDI2, the enzyme responsible for AMOT cleavage, is indispensable for retinal vascular development, and the defective angiogenesis in *Ddi2*$^{iEC\text{-}KO}$ retinas is likely due to the absence of AMOT-CT.

### NF2-regulated AMOT cleavage is essential for retinal angiogenesis

The process of AMOT cleavage by DDI2 is tightly regulated by NF2 (Fig 3L). We then established EC-specific *Nf2*-KO (*Nf2*$^{iEC\text{-}KO}$) by crossing *Nf2*$^{fl/fl}$ mice with *Cdh5*-creERT2 mice (Wang *et al*, 2021; Fig 8A). Retinal angiogenesis in *Nf2*$^{iEC\text{-}KO}$ mice was severely impaired as indicated by robust reduction of vascular area (Fig 8B and C). Strikingly, many ECs were accumulated at the migration front and formed a dense vascular network (Figs 8D and EV4E). Cell density and branch points at the angiogenic front of *Nf2*$^{iEC\text{-}KO}$ retinas were also increased, sprout length was decreased, and sprout numbers were largely unchanged (Fig 8E). The vascular network between artery and vein was deformed in *Nf2*$^{iEC\text{-}KO}$ retinas, especially at regions close to optic stalk (Fig 8D). Moreover, the average filopodia length was also largely reduced (Fig 8F and G). These results suggest that NF2 is also required for retinal angiogenesis.

To test whether the AMOT cleavage pathway is involved in the impaired angiogenesis in *Nf2*$^{iEC\text{-}KO}$ *retinas*, we established mouse lines that could simultaneously delete *Nf2* and express *AMOT-CT* (*Nf2*$^{iEC\text{-}KO}$; *CT*$^{iEC\text{-}TG}$) or *AMOT-Δcut* (*Nf2*$^{iEC\text{-}KO}$; *Δcut*$^{iEC\text{-}TG}$) in ECs (Fig 8A). Interestingly, the aberrant retinal vascular development, especially EC migration defects caused by *Nf2* deficiency, were completely normalized upon AMOT-CT but not AMOT-Δcut expression (Fig 8B–E). In addition, AMOT-CT also rescues the morphological defects of tip cells, both in terms of the number and length of filopodia (Fig 8F and G). Hence, the function of NF2 in retinal angiogenesis is largely mediated by AMOT cleavage and the generation of AMOT-CT.

Both *Ddi2*$^{iEC\text{-}KO}$ and *Nf2*$^{iEC\text{-}KO}$ retinas exhibited impaired angiogenesis, but the phenotype of *Nf2*$^{iEC\text{-}KO}$ retinas appeared to be more complex (Figs 7D and 8D). We reasoned that NF2 regulates both AMOT cleavage and YAP/TAZ activity (Appendix Fig S7F; Hamaratoglu *et al*, 2006; Zhang *et al*, 2010; Qi *et al*, 2022). Thus, in Nf2$^{iEC\text{-}KO}$ retinas, YAP/TAZ activity was likely upregulated to drive ectopic EC proliferation (Fig 8H and I). On the other hand, DDI2 did not regulate YAP/TAZ activity, and hyperproliferation of ECs was not observed in *Ddi2*$^{iEC\text{-}KO}$ retinas (Fig 7H and I). Interestingly, the distribution of proliferating cells was normalized by both AMOT-Δcut and AMOT-CT in *Nf2*-KO retinas (Fig 8H and I). *Nf2*-deficient cells with YAP/TAZ hyperactivation might be more sensitive to AMOT perturbation, hence there could be a mild inhibition of cell proliferation by AMOT-Δcut and AMOT-CT (Fig 8H and I). Similar effect of AMOT on the proliferation of *NF2*-null cancer cells had been reported previously (Wang *et al*, 2021).

### AMOT cleavage is involved in pathological angiogenesis

Angiogenesis is also involved in diverse pathological conditions, such as tissue regeneration and tumorigenesis (Carmeliet, 2003). Retinal angiogenesis is sensitive to different stresses, such as oxygen-induced retinopathy (OIR) that frequently occurs in preterm infants. In some cases, the vascular injury caused by high oxygen cannot be fully repaired and undergoes pathological neovascularization (NV). The pathological process of OIR can be faithfully modeled in mice, in which neonatal pups are exposed to 75% oxygen for 5 days (P7–P12) to induce vascular obliteration and then return to room air to initiate regrowth of retinal vessels until P15–P17 (Connor *et al*, 2009; Stahl *et al*, 2010; Fig 9A). Several genetic manipulations, such as *CT*$^{iEC\text{-}TG}$ and *Δcut* KI, showed weak effects on physiological angiogenesis (Figs 6 and EV3). We thought that their effects on angiogenesis under stressed conditions might be more robust. Interestingly, we found that the retinas of mice under OIR treatment expressed more AMOT-CT, indicating that AMOT cleavage occurred during pathological angiogenesis (Fig EV5A and B). Furthermore, In OIR model, *CT*$^{iEC\text{-}TG}$ retinas exhibited decreased avascular area and much more sprouts from the damaged veins compared with control mouse retinas (Fig 9B and C). By contrast, *Δcut* KI retinas showed severe inhibition of revascularization, as characterized by a significant increase of avascular area and fewer sprouts from veins (Fig 9D and E). These data suggest that the pathological retinal angiogenesis is inhibited by uncleavable AMOT whereas promoted by AMOT-CT.

## Discussion

In this study, we have uncovered a signaling pathway regulating cleavage and activation of AMOT. Upon LPA stimulation, NF2, TNKS1/2, RNF146, and DDI2, lead to membrane localization, PARylation, ubiquitination, and cleavage of AMOT, respectively. Moreover, we have demonstrated a robust effect of the AMOT cleavage pathway on both physiological and pathological angiogenesis, in zebrafish and mice.

 

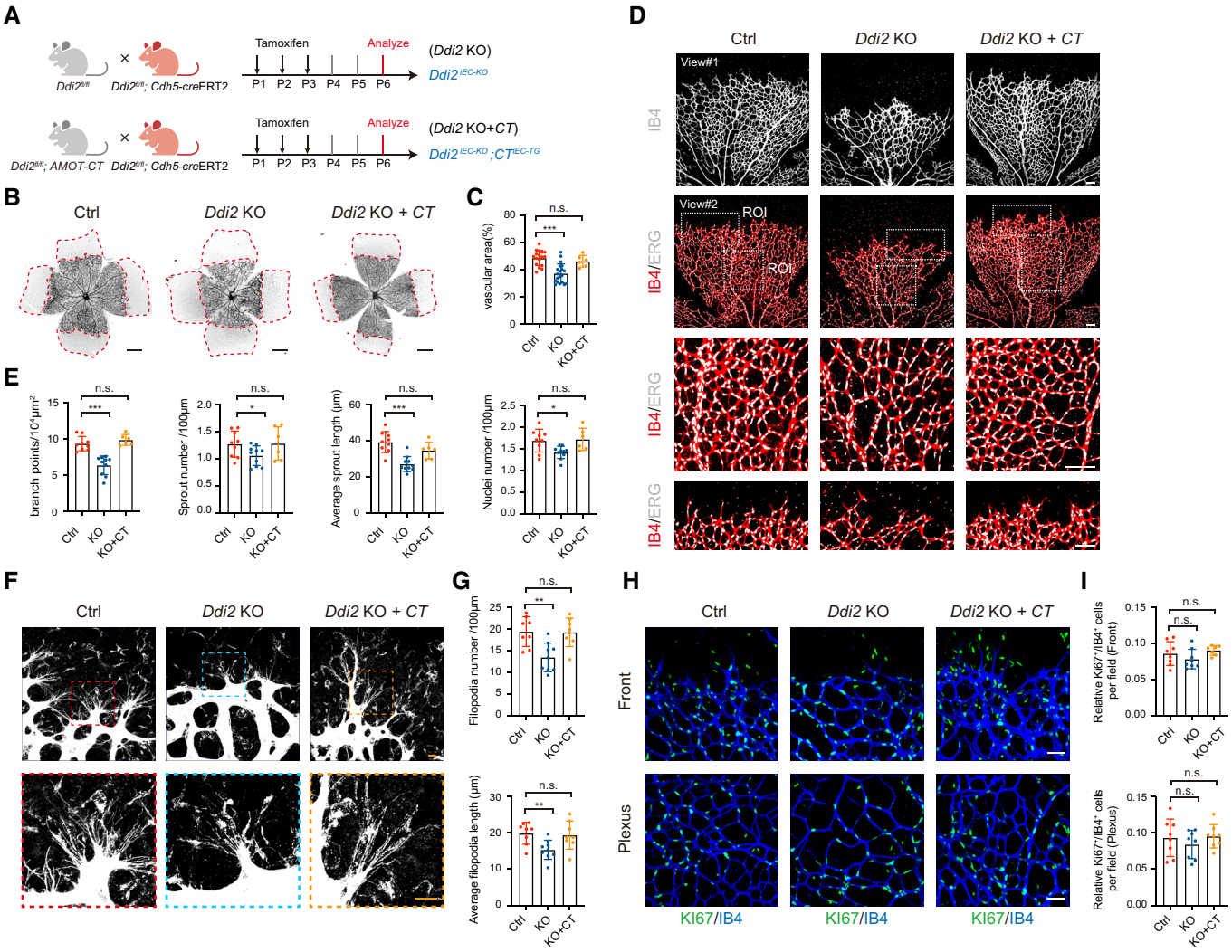


**Figure 7. AMOT-CT rescues vascular defects in *Ddi2* deficient mouse retinas.**

A Left, schematic diagram of the generation of endothelial-specific *Ddi2* knockout ($Ddi2^{iEC\text{-}KO}$) mice and *Ddi2* knockout, *AMOT-CT* overexpression ($Ddi2^{iEC\text{-}KO}$; $CT^{iEC\text{-}TG}$) mice. Right, experimental strategy to assess retinal vascularization at P6. All mice were treated with tamoxifen at P1,2,3 and analyzed at P6.

B, C $Ddi2^{iEC\text{-}KO}$ mice show reduced retinal vascular area at P6 while *AMOT-CT* overexpression can partially rescue the phenotype. IB4 staining of the whole retina (B). Quantification of the vascular area of P6 retinas (C). Scale bar: 500 μm. Each dot represents one retina, control ($n$ = 17), $Ddi2^{iEC\text{-}KO}$ ($n$ = 20), and $Ddi2^{iEC\text{-}KO}$; $CT^{iEC\text{-}TG}$ ($n$ = 6).

D $Ddi2^{iEC\text{-}KO}$ mice show delayed retinal angiogenesis. Immunofluorescent images of whole-mount retinas stained for IB4 and ERG of control, $Ddi2^{iEC\text{-}KO}$, and $Ddi2^{iEC\text{-}KO}$; $CT^{iEC\text{-}TG}$ mice at P6. White dash rectangles indicate regions of interest (ROI) are shown below at higher magnification. Scale bar: 100 μm.

E Quantification of the retinal vasculature of control, $Ddi2^{iEC\text{-}KO}$, and $Ddi2^{iEC\text{-}KO}$; $CT^{iEC\text{-}TG}$ retinas. Each data point represents the average of two or three measurements from one retina, Control ($n$ = 9), $Ddi2^{iEC\text{-}KO}$ ($n$ = 10), and $Ddi2^{iEC\text{-}KO}$; $CT^{iEC\text{-}TG}$ ($n$ = 6).

F High magnification confocal images of filopodia extension at the leading edge of the P6 retina. Tip cells are labeled with IB4. Scale bar: 10 μm.

G Quantification of the number and average length of filopodia in control ($n$ = 8), $Ddi2^{iEC\text{-}KO}$ ($n$ = 9), and $Ddi2^{iEC\text{-}KO}$; $CT^{iEC\text{-}TG}$ ($n$ = 8) P6 retinal sprouts. Each data point represents the average of three measurements from one retina.

H, I Representative images and comparisons of Ki67 positive endothelial cells in control ($n$ = 8), $Ddi2^{iEC\text{-}KO}$ ($n$ = 8), and $Ddi2^{iEC\text{-}KO}$; $CT^{iEC\text{-}TG}$ ($n$ = 7) P6 retinas. Each data point represents the average of three measurements from one retina. Scale bar: 50 μm.

Data information: Data are shown as mean ± SEM from at least three independent littermates. Statistical significance was determined using the Student's $t$-test, $^*P < 0.05$, $^{**}P < 0.01$, $^{***}P < 0.001$, n.s. indicates not significant.
Source data are available online for this figure.

It has been shown previously that *Amot* deletion in mouse ECs inhibited tip cells and impaired radial vessel expansion, suggesting that AMOT is required for angiogenesis (Zhang *et al*, 2021). However, we have shown that uncleavable AMOT inhibits, whereas AMOT-CT generated following AMOT cleavage is indispensable for retinal angiogenesis (Figs 6–9). In addition, regulators of AMOT cleavage, such as DDI2 and NF2, are required for angiogenesis, and AMOT-CT expression rescued vascular defects caused by *Ddi2* or

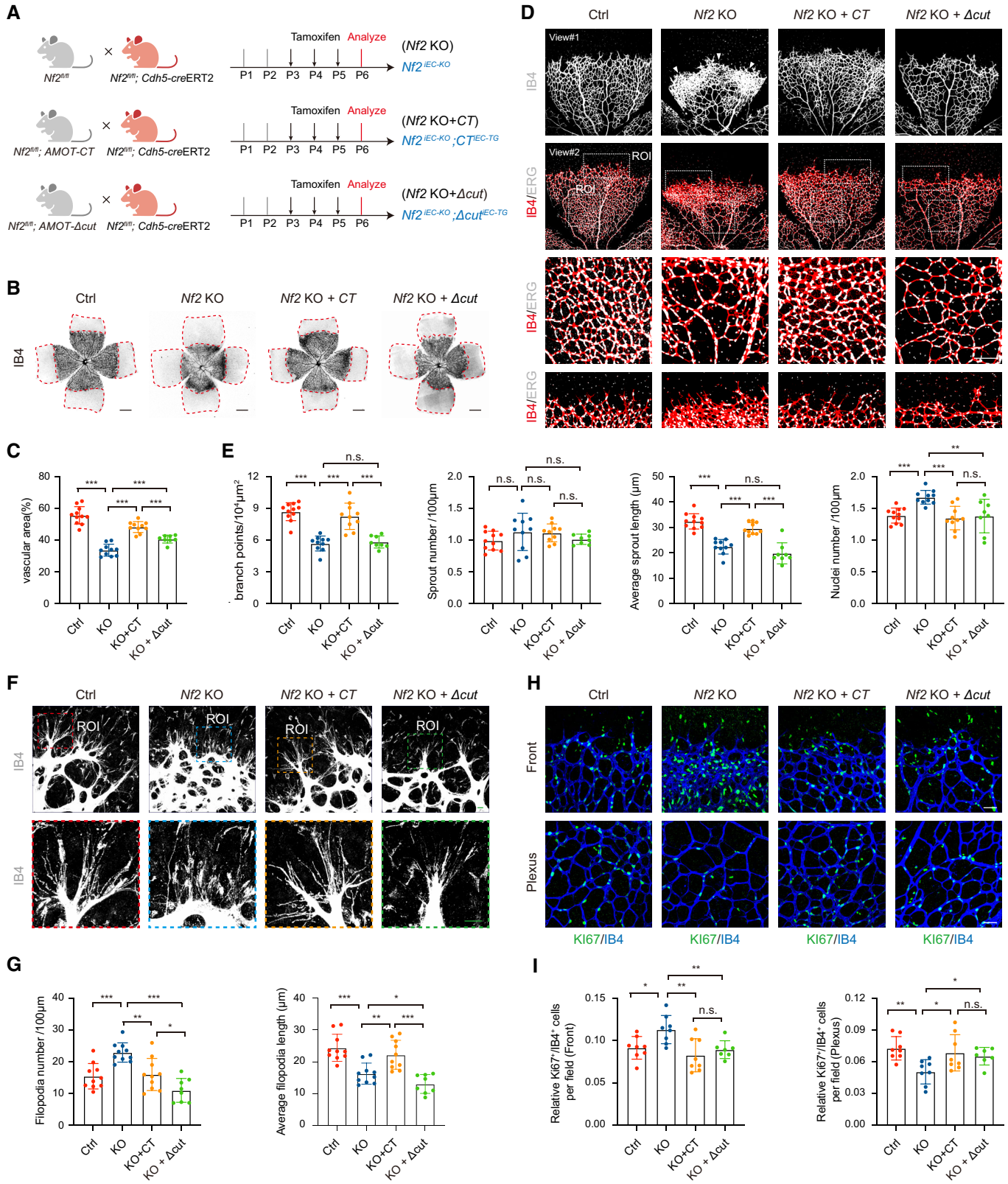


**Figure 8.**

**Figure 8. AMOT-CT rescues vascular defects in *Nf2*-deficient mouse retinas.**

A Left, schematic diagram of the generation of endothelial-specific *Nf2* knockout ($Nf2^{iEC\text{-}KO}$), *Nf2* knockout with *AMOT-CT* overexpression ($Nf2^{iEC\text{-}KO}$; $CT^{iEC\text{-}TG}$), and *Nf2* knockout with *AMOT-Δcut* overexpression ($Nf2^{iEC\text{-}KO}$; $\Delta cut^{iEC\text{-}TG}$) mice. Right, experimental strategy to assess retinal vascularization at P6. All mice were treated with tamoxifen at P3,4,5 and analyzed at P6.

B, C $Nf2^{iEC\text{-}KO}$ mice show reduced retinal vascular area while *CT* overexpression can partially rescue the phenotype. IB4 staining of the whole retina (B). Quantification of the vascular area of P6 retinas (C). Scale bar: 500 μm. Each dot represents one retina, control ($n$ = 11), $Nf2^{iEC\text{-}KO}$ ($n$ = 10), $Nf2^{iEC\text{-}KO}$; $CT^{iEC\text{-}TG}$ ($n$ = 10), and $Nf2^{iEC\text{-}KO}$; $\Delta cut^{iEC\text{-}TG}$ ($n$ = 8).

D $Nf2^{iEC\text{-}KO}$ retinas show endothelial cell accumulation in the sprouting front and sparse vascular plexus in the region close to optic stalk. *CT* overexpression can partially rescue the phenotype. Immunofluorescent images of whole-mount P6 retinas stained for IB4 and ERG are shown. White rectangles indicate regions of interest (ROI). Scale bar: 100 μm.

E Quantification of retinal vessels in P6 retinas. Each data point represents the average of two or three measurements from one retina, control ($n$ = 11), $Nf2^{iEC\text{-}KO}$ ($n$ = 10), $Nf2^{iEC\text{-}KO}$; $CT^{iEC\text{-}TG}$ ($n$ = 10), and $Nf2^{iEC\text{-}KO}$; $\Delta cut^{iEC\text{-}TG}$ ($n$ = 8).

F, G High magnification confocal images and quantification of filopodia extension at the leading edge of the P6 retinas. Tip cells are labeled with IB4. Scale bar: 10 μm. Control ($n$ = 10), $Nf2^{iEC\text{-}KO}$ ($n$ = 10), $Nf2^{iEC\text{-}KO}$; $CT^{iEC\text{-}TG}$ ($n$ = 10), and $Nf2^{iEC\text{-}KO}$; $\Delta cut^{iEC\text{-}TG}$ ($n$ = 8).

H, I Representative images and comparisons of Ki67 positive endothelial cells in control ($n$ = 8), $Nf2^{iEC\text{-}KO}$ ($n$ = 8), $Nf2^{iEC\text{-}KO}$; $CT^{iEC\text{-}TG}$ ($n$ = 8), and $Nf2^{iEC\text{-}KO}$; $\Delta cut^{iEC\text{-}TG}$ ($n$ = 7) P6 retinas. Each data point represents the average of three measurements from one retina. Scale bar: 50 μm.

Data information: Data are shown as mean ± SEM from at least three independent littermates. Statistical significance was determined using the Student's *t*-test, $^{*}P < 0.05$, $^{**}P < 0.01$, $^{***}P < 0.001$, n.s. indicates not significant.
Source data are available online for this figure.

*Nf2* deficiency (Figs 7 and 8). It is likely that *Amot* KO not only deleted AMOT but also abolished AMOT-CT, hence leading to vascular defects. Moreover, LPA stimulation leads to the destabilization of AMOT family proteins (Dai *et al*, 2013; Adler *et al*, 2013b; Wang *et al*, 2021), but the deletion of LPA producing-enzymes or LPA receptors also impaired angiogenesis, in a manner similar to *Amot* KO (van Meeteren *et al*, 2006; Sumida *et al*, 2010; Yukiura *et al*, 2011). Our findings suggest that when LPA signaling is blocked, the generation of AMOT-CT is inhibited, which in turn delays vascular development. Together, these data indicate that the generation of AMOT-CT, rather than AMOT expression, determines the efficiency of angiogenesis.

AMOT and NF2 are components of the Hippo pathway, and LPA has been identified as an upstream signal of the Hippo pathway (Yu *et al*, 2012). AMOT is also a substrate of LATS1/2, and phosphorylation of AMOT by LATS1/2 disrupts the interaction between AMOT and actin cytoskeleton and impairs cell migration (Chan *et al*, 2013; Dai *et al*, 2013; Adler *et al*, 2013b; Mana-Capelli *et al*, 2014). However, LPA-evoked and NF2-regulated cleavage of AMOT is clearly separated from the canonical Hippo pathway. First, AMOT cleavage occurs in cells deficient in most Hippo pathway genes, such as *MST1/2*, *LATS1/2*, and *SAV1* (Fig 3F). Second, both full-length AMOT and AMOT-CT inhibit YAP/TAZ activity. Hence, the signaling cascade regulating AMOT cleavage may be referred to as a Hippo-related pathway. We propose that, downstream of LATS1/2 and NF2, YAP/TAZ serve as regulators of cell proliferation, whereas AMOT family proteins may mainly control cell migration in angiogenesis.

VEGF and hypoxia signaling pathways play critical roles in both physiological and pathological angiogenesis (Pugh & Ratcliffe, 2003; Krock *et al*, 2011; Shibuya, 2011; Apte *et al*, 2019). It is currently unknown if VEGF and hypoxia signalings are involved in the proangiogenic role of AMOT-CT. Preliminary data suggest that HIF1-a expression and VEGFR2 phosphorylation are not affected in cells expressing ectopic AMOTp130, AMOT-CT, or AMOT-Δcut, hence AMOT, regardless of cleaved or not, does not directly modulate VEGF and hypoxia signalings. In future, it would be interesting to investigate whether VEGF and hypoxia signalings are modulated by AMOT cleavage *in vivo*.

**Figure 9. AMOT cleavage promotes pathological angiogenesis.**

A Cartoon schematic of a mouse oxygen-induced retinopathy (OIR) model. Neonatal pups and nursing mothers were kept in room air from P0 to P7 and exposed to 75% oxygen from P7 to P12, then returned to room air. High oxygen caused severe vessel loss and the avascular retina became hypoxic, which led to normal vessel regrowth and pathological neovascular response, neovascularization reached a maximum at P17. (Connor *et al*, 2009). For $CT^{iEC\text{-}TG}$ group, the retinas were harvested at P15 to see the "stimulatory" effect of AMOT-CT, while for *Δcut* KI group, the retinas were harvested at P17 to see the "inhibitory" effect of uncleavable AMOT. For $CT^{iEC\text{-}TG}$ group, mice were treated with tamoxifen at P3,4,5.

B *CT* overexpression promotes revascularization in the OIR model. Upper, IB4 staining of the whole retina of P15 control and $CT^{iECTG}$ mice after OIR. Lower, higher magnification images of sprouting vessels from veins. Scale bars are shown in the figures.

C Quantification of mouse weight, avascular area in the whole retina and vessel sprouting coverage in the red stippled area. Mice with similar body weights were chosen to compare the angiogenesis status. All the pups were weighted at P15 before being sacrificed. For body weight, each dot represents one mouse, control ($n$ = 10), and $CT^{iECTG}$ ($n$ = 8). For avascular area, each data point represents one retina, control ($n$ = 20), and $CT^{iECTG}$ ($n$ = 15). For sprouting area, each data point represents the average of two or three measurements from one retina, control ($n$ = 13), and $CT^{iECTG}$ ($n$ = 12).

D Blocking AMOT cleavage inhibits revascularization in the OIR model. Upper, IB4 staining of the whole retina of P17 WT and *Δcut* KI mice after OIR. Lower, higher magnification images of sprouting vessels from veins. Scale bars are shown in the figures.

E Quantification of mouse weight, avascular area in the whole retina, and vessel sprouting coverage in the red stippled area. All the pups were weighted at P17 before being sacrificed. For body weight, each dot represents one mouse, control ($n$ = 15), and *Δcut* KI ($n$ = 12). For avascular area, each data point represents one retina, control ($n$ = 30), and *Δcut* KI ($n$ = 24). For sprouting area, each data point represents the average of two or three measurements from one retina, control ($n$ = 20), and *Δcut* KI ($n$ = 19).

Data information: Data are shown as mean ± SEM. Statistical significance was determined using the Student's *t*-test, $^{*}P < 0.05$, $^{**}P < 0.01$, $^{***}P < 0.001$, n.s. indicates not significant.
Source data are available online for this figure.

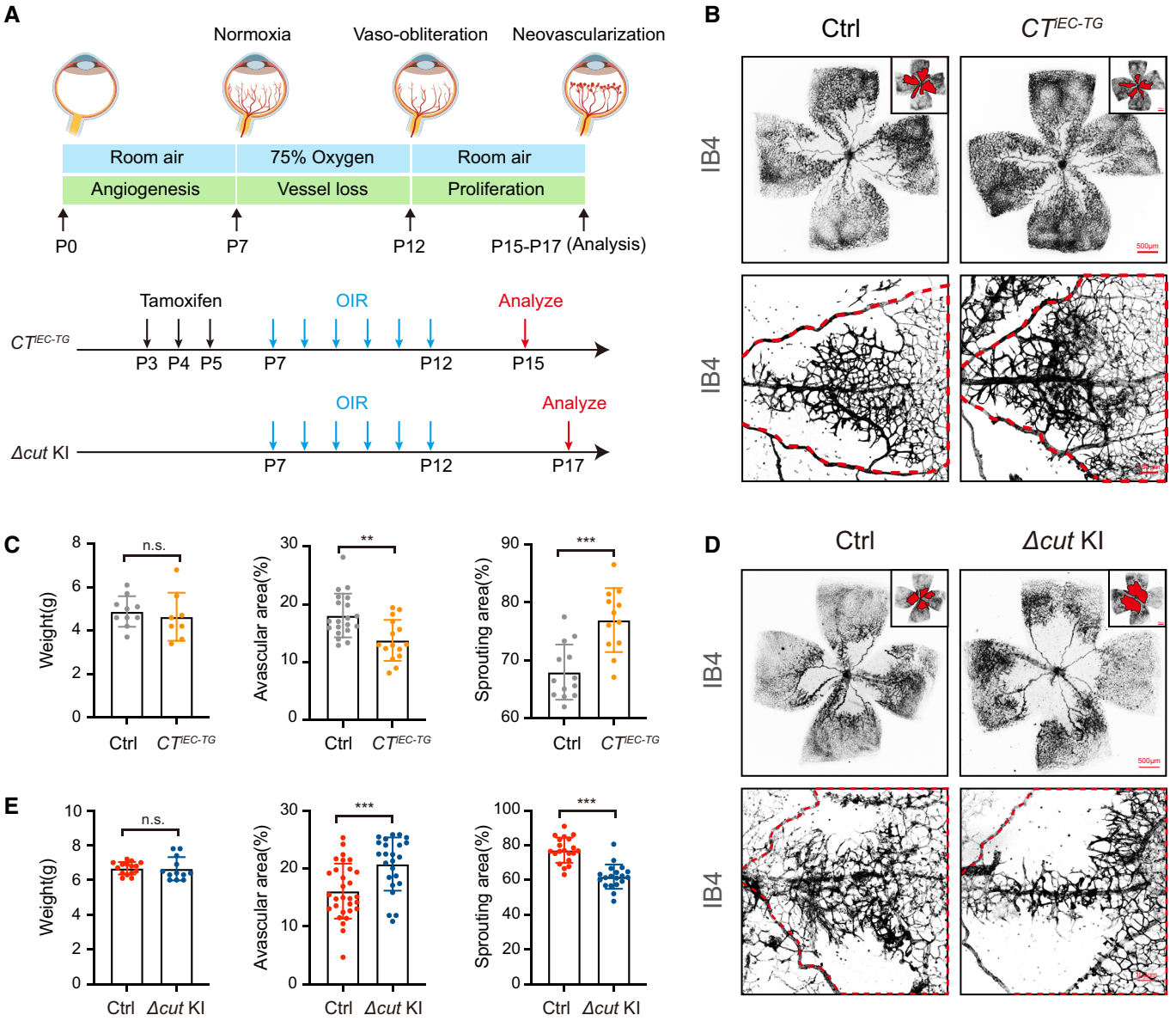


**Figure 9.**

The generation of AMOT-CT appears to be a rapid and transient process (Fig 1). In biology, the production of unstable active mediators via proteolysis is not rare. For instance, nuclear factor erythroid 2-Like 1 (NRF1, the only reported DDI2 substrate) is constantly cleaved and rapidly degraded, and the active fragment accumulates upon proteasome inhibition to induce target gene expression (Koizumi *et al*, 2016; Lehrbach & Ruvkun, 2016; Gu *et al*, 2020). Notch intracellular domain (NICD), the proteolytic product of Notch proteins, also undergoes rapid turnover, and its stabilization is essential for inhibiting angiogenesis (Tetzlaff *et al*, 2004; Tsunematsu *et al*, 2004; Lim *et al*, 2019). The immediate accumulation of proteolytic products in the presence of upstream signals is critical for the regulation of biological processes at both spatial and temporal resolutions, and the production of AMOT-CT and NICD provides a flexible switch for precise regulation of angiogenesis.

AMOT is expressed in many cell types, such as neurons, glial cells, and certain epithelial cells. Therefore, other than angiogenesis, the AMOT cleavage pathway may also be involved in diverse physiological and pathological processes, such as neurogenesis, regeneration, and tumorigenesis. It would be interesting to explore the additional biological functions of AMOT-CT. Moreover, multiple enzymes involved in AMOT cleavage may be pharmacologically targeted to treat aberrant angiogenesis and related diseases.

## Materials and Methods

### Antibodies

The following antibodies were used in this study: anti-AMOT (A303-305A) was from Bethyl Laboratories. Anti-AMOT (SC-166924), anti-TNKS1/2

 

**Table 1. Mouse strains used in this study.**

| Mouse strain | Genotype | Specific description | Validation |
|---|---|---|---|
| *Δcut*$^{iEC\text{-}TG}$ | ***R26****-e(CAG-LSL-mNeoGreen-FLAG-AMOT-Δ131132aa); Cdh5-creERT2* | **Overexpress** human *AMOT-Δcut* (with amino acids F131- and Y132-deleted) in endothelial cells | Immunofluorescence staining (Appendix Fig S4E) |
| *CT*$^{iEC\text{-}TG}$ | ***R26****-e(CAG-LSL-mNeoGreen-FLAG-AMOT-132–1084aa); Cdh5-creERT2* | **Overexpress** human *AMOT-CT* in endothelial cells | Immunofluorescence staining (Appendix Fig S5E) |
| *Δcut* KI | *Amot-e(c.394-399del)1* | *AMOT-Δcut* **knockin (KI)** mice (with F132 and Y133 of mouse AMOT deleted) | Immunoblotting (Appendix Fig S6E) |
| *Ddi2*$^{iEC\text{-}KO}$ | *Ddi2*$^{flox/flox}$*; Cdh5-creERT2* | **Knockout** *Ddi2* in endothelial cells | qPCR (Appendix Fig S9E) |
| *Ddi2*$^{iEC\text{-}KO}$*; CT*$^{iEC\text{-}TG}$ | *Ddi2* $^{flox/flox}$*; R26-e(CAG-LSL-mNeoGreen-FLAG-AMOT-132–1084aa); Cdh5-creERT2* | **Knockout** *Ddi2* and **overexpress** human *AMOT-CT* in endothelial cells | Genotyping |
| *Nf2*$^{iEC\text{-}KO}$ | *Nf2*$^{flox/flox}$*; Cdh5-creERT2* | **Knockout** *Nf2* in endothelial cells | immunoblotting (Wang *et al*, 2021) |
| *Nf2*$^{iEC\text{-}KO}$*; CT*$^{iEC\text{-}TG}$ | *Nf2* $^{flox/flox}$*; R26-e(CAG-LSL-mNeoGreen-FLAG-AMOT-132–1084aa); Cdh5-creERT2* | **Knockout** *Nf2* and **overexpress** human *AMOT-CT* in endothelial cells | Genotyping |
| *Nf2*$^{iEC\text{-}KO}$*; Δcut*$^{iEC\text{-}TG}$ | *Nf2* $^{flox/flox}$*; R26-e(CAG-LSL-mNeoGreen-FLAG-AMOT-Δ131132aa); Cdh5-creERT2* | **Knockout** *Nf2* and **overexpress** human *AMOT-Δcut* in endothelial cells | Genotyping |

(SC-8337), anti-Ubiquitin (SC-9133), and anti-YAP/TAZ (SC-101199) antibodies were from Santa Cruz Biotechnology. Anti-MST2 (ab52641), anti-ERG (ab92513), and anti-AMOTL2 (ab135722) antibodies were from Abcam. Anti-RNF146 (H00081847-B01P) antibody was from Abnova. Anti-HSP90 (610418) and anti-CD31 (553370) antibodies were from BD Bioscience. Anti-HA-HRP conjugate (14031S), anti-LATS1 (3477S), anti-LATS2 (5888S), anti-Merlin (12888S), anti-MST1 (3682S), anti-SAV1 (13301S), anti-MOB (13730S), anti-YAP (14074S), and anti-pYAP (13008S) antibodies were from Cell Signaling Technology. Anti-pan-ADPr (MABE1016) antibody was from Millipore. Anti-DDI2 (HPA043119), anti-AMOTL1 (HPA001196), anti-FLAG (F7425), and anti-FLAG-HRP conjugate (A8592) antibodies were from Sigma-Aldrich. mNeonGreen (32F6) antibody was purchased from Proteintech. Anti-VE-Cadherin was from ThermoFisher (14-1441-82). Anti-pAMOTS175 antibody was kindly provided by Dr. Wanjin Hong. Anti-AMOT (N-terminal) antibody was raised by immunizing rabbits with human AMOTp130 (amino acids 1–123, Cloud-Clone Corp).

### Chemicals

The following chemicals were used in this study: EGF (AF-100-15, Peprotech), Heprain (2812/100, Tocris), VEGF (293-VE/CF, R&D Systems), and bFGF (R&D Systems). Bortezomib (S1013), Olaparib (S1060), and the protease inhibitor library (L2500) were purchased from Selleck. The detailed information about the inhibitor library is shown in Appendix Table S1. XAV939 (X3004-5MG), LPA (L7260-5MG), S1P (73914-1MG), MG132 (C2211-5MG), and insulin (I-1882) were from Sigma-Aldrich. Alexa-Fluor-conjugated Isolectin B4 (121411 and 121412) were from Invitrogen.

### Cell culture

HEK293A, HEK293T, MDCK, MEF, SW620, RKO, RCC4, 769-P, NCI-H2452, NCI-H2052, MESO-12, MESO-22 and MESO-25 cells were maintained in DMEM media (Corning). U2OS, ACHN, and NCI-H2373 cells were maintained in RPMI1640 media (Corning). HCT15 and HCT116 cells were cultured in DMEM/F12 media (Corning). All media were supplemented with 10% fetal bovine serum (FBS, Gibco) and 50 mg/ml penicillin/streptomycin (SV30010, Hyclone). HUVECs (C-12203, PromoCell) were grown in endothelial cell growth medium (C-22010, PromoCell) and were cultured up to passage 5 for all experiences. The human microvascular endothelial cell line (HMEC1) was maintained in MCDB 131 medium (10372019; ThermoFisher) supplemented with 10% FBS, 10 mmol/l L-glutamine, 10 ng/ml epidermal growth factor, and 1 μg/ml hydrocortisone. For the primary culture of mouse endothelial cells, the cells were isolated using CD31 MicroBeads (130-097-418; Miltenyi Biotech) according to the manufacturer's instructions and were cultured in Endothelial Cell Growth Medium (C-22010, PromoCell) for 24 h, and adherent cells were subjected to further analysis. All endothelial cells were cultured on type I collagen (Corning) coated dishes or plates. Cells were incubated at 37°C with 5% $CO_2$.

### Plasmids and transfection

To generate the expression constructs, the open reading frames (ORFs) were amplified from a human cDNA library and cloned in frame into pLVX vector (632164, Takara) using NEB Gibson Assembly® Master Mix Assembly (E2611, NEB) or ClonExpress MultiS One Step Cloning Kit (C113-02, Vazyme). For CRISPR/Cas9 cloning, sgRNA oligos were cloned into the pSpCas9(BB)-2A-Puro (PX459) V2.0 or lentiCRISPR v2 vectors (provided by Dr. Feng Zhang) using T4 ligase (2011A, Takara). All constructs were validated by Sanger sequencing. Expression of recombinant proteins was confirmed by Western blotting. Plasmid DNA transfection was performed using PEI (1 mg/ml, pH 7.0; 23966-2, Polysciences Inc) or PolyJet Transfection Reagent (SL100688, Signagen Laboratories) according to the manufacturer's instructions. siRNAs were purchased from GenePharma. The detailed sequence information is as follows: siDDI2-1: 5′-GCAAAGTGAATGGACATCCTGTGAA-3′; siDDI2-2: 5′-GCTTGGACAATCCAGCCTT-3′; siNF2-1: 5′-CAGCCTGTCTTTCGACTTCAA-3′; siNF2-2: 5′-GGACAAGAAGGTACTGGAT-3′; siRNF146-1: 5′-GGATGTATCTGCAGTTGTT-3′; siRNF146-2: 5′-CCCGATCGATC

AGATCGAT-3′. siRNA transfection was performed using Lipofectamine RNAiMAX Reagent (13778075, ThermoFisher).

#### Lentiviral production and infection

Lentivirus was produced by co-transfecting pLVX or lentiCRISPR v2 vector with packaging vectors psPAX2 and pMD2.g into HEK293T cells. Two days later, the medium containing virus was harvested and filtered through a 0.45 μm filter (SLHP033RS, Millipore), and the virus was concentrated by ultracentrifugation. Cells were infected with virus in the presence of 10 μg/ml polybrene (TR-1003-G, Sigma-Aldrich). At 48 h after infection, stable cells were selected with 2 μg/ml puromycin (ant-pr-1, Invivogen).

#### Generation of knockout cell lines

The CRISPR/Cas9 system was applied to delete specific genes in HEK293A cells. Small guide RNA (sgRNA) sequences were designed using CRISPR design tool at http://www.e-crisp.org/E-CRISP/ and cloned into the plasmid pSpCas9(BB)-2A-Puro (PX459) V2.0 (Addgene #62988) or lentiCRISPR v2 (52961, Addgene) kindly provided by Dr. Feng Zhang. The sgRNA sequences targeting all the aspartic proteases are listed in Appendix Tables S2 and S3. Other sgRNA sequences were used as described previously (Wang *et al*, 2021). To generate single cell clones, transfected cells were selected with 2 μg/ml puromycin for 48 h and then sorted into 96-well plates with one cell in each well. The clones were screened by Western blotting and confirmed by DNA sequencing. The genomic DNA sequences of *AMOT* KO, *AMOT/L1/L2*-tKO, *TNKS1/2*-dKO, *RNF146*-KO, and *LPAR1-3*-tKO knockout cell lines were described previously (Wang *et al*, 2021). *NF2*-KO, *SAV1*-KO, *MST1/2*-dKO, *LATS1/2*-dKO, *MOB1A/B*-dKO, and *MST1/2-MAP4Ks*-9KO cells were described previously (Meng *et al*, 2015; Plouffe *et al*, 2016; Qi *et al*, 2022).

#### Western blotting

Cell lysates were denatured by boiling at 95°C for 5 min in SDS loading buffer (50 mM Tris–HCl at pH 6.8, 2% SDS, 10% glycerol, 0.025% bromophenol blue and β-mercaptoethanol). Proteins were separated by sodium dodecyl sulfate-polyacrylamide gel electrophoresis (SDS–PAGE) and electro-transferred onto nitrocellulose membranes. After blocking with 5% nonfat milk at room temperature for 1 h, the membranes were hybridized with indicated primary antibodies in 5% bovine serum albumin (BSA) overnight at 4°C and then secondary antibodies in 5% milk for 1 h at room temperature. Protein bands were visualized using High-sig ECL Western Blotting Substrate (Tanon, #180-501), and chemiluminescence was detected using the Tanon 5200S imaging system. Quantification of the intensity of the protein bands was performed using ImageJ software (NIH).

#### Immunoprecipitation

Cultured cells were lysed in ice-cold RIPA buffer containing 50 mM HEPES at pH 7.5, 150 mM NaCl, 1% NP-40, 0.1% SDS, 0.5% sodium deoxycholate, 1 mM PMSF, protease inhibitor cocktail (HY-K0010, MCE), and phosphatase inhibitors (HY-K0021; HY-K0022, MCE). Cell lysates were centrifuged at 13,500 *g* for 15 min at 4°C, and the supernatants were used for immunoprecipitation. Supernatants were incubated with the primary antibody for 1 h at 4°C. Protein A beads were then added and incubated for an additional 2 h. For IP of FLAG-tagged proteins, anti-FLAG M2 affinity agarose beads (A2220, Sigma-Aldrich) were used. Beads were washed four times with ice-cold RIPA buffer. Immunoprecipitated proteins were eluted with SDS loading buffer at 95°C for 5 min. The immunoprecipitated proteins were then separated by SDS–PAGE and analyzed by immunoblotting.

#### Immunofluorescence staining

Cells cultured on fibronectin-coated coverslips were used for immunofluorescence staining. Cells were washed with PBS three times, fixed with 4% paraformaldehyde for 15 min, then permeabilized with 0.2% Triton X-100 for 10 min. After blocking with 3% bovine serum albumin and 3% goat serum in PBS for 1 h at room temperature, cells were stained with primary antibodies overnight at 4°C. Cells were then washed three times and incubated with Alexa-Fluor 488, 555, or 647 conjugated secondary antibodies (ThermoFisher) for 1 h at room temperature. Slides were washed and mounted with ProLong™ Gold Antifade Mountant with DAPI (P36935, ThermoFisher). Images were captured with a Leica SP8 confocal microscope or ZEISS LSM 900 confocal microscope with Airyscan 2.

#### 5′ ethynyl-2′-deoxyuridine (EdU) staining

EdU incorporation assay was carried out by using a 12-well glass-bottom plate (P12-1.5H-N, Cellvis) coated with fibronectin. Briefly, $2 \times 10^5$ cells were seeded in one well and allowed to attach overnight. Cells were incubated with 10 μM EdU in complete media for 2 h at 37°C. After EdU incubation, cells were washed with PBS and fixed in 4% paraformaldehyde for 15 min, then permeabilized with 0.2% Triton X-100 for 10 min. Proliferating cells that incorporate EdU were detected with EdU Imaging Kits (K1075, APExBio) according to the manufacturer's instructions. DAPI staining was used to visualize the nuclei. Images were captured with a ZEISS LSM 900 confocal microscope with Airyscan 2. The numbers of EdU-positive and DAPI-positive nuclei were counted automatically using the Image Analysis program in ZEISS ZEN3.1 software.

#### Transwell cell migration assay

HUVEC or HMEC1 cells ($1 \times 10^4$ cells suspended in 100 μl medium containing 0.1% FBS) were seeded in the transwell insert (3422, Corning) with 20% FBS medium in the bottom wells as a chemoattractant. After incubation for 24 h at 37°C, cells were fixed with 4% formalin and stained with violet solution (V5265-500ML, Sigma), the nonmigrated cells on the upper side were removed with a cotton swab. Migrated cells were photographed and quantified.

#### HUVEC spheroid-based sprouting angiogenesis assay

HUVEC spheroid-based sprouting angiogenesis assay was performed as previously described (Tetzlaff & Fischer, 2018). $8 \times 10^4$ HUVEC cells were resuspended in 4 ml Endothelial Cell Growth Medium (C-22010, PromoCell), and mixed with 1 ml methyl cellulose carefully.

 

The entire mixture was pipetted in 25 μl hanging droplets onto a 10 cm dish and incubated upside-down for 24 h for spheroid formation. The spheroids were rinsed with PBS and resuspended in 2 ml of methocel containing 20% FBS. Collagen type I from rat tails (354236 and 354249, Corning) and 10 × Medium 199 (M9163, Sigma) were mixed on ice, and the pH was adjusted to 7.4 using 0.1 N NaOH. Two milliliter of this mixture was added to the spheroid suspension and the final concentration of collagen is 2 mg/ml. One milliliter of the spheroid-collagen solution was pipetted into a 35-cm glass-bottom culture dish (D35-20-1-N, Cellvis) and incubated at 37°C for 30 min. After polymerization of the collagen gel, 1 ml culture medium containing 25 ng/ml VEGF was added to the dish. The spheroids were incubated for a further 18 h and fixed with 4% paraformaldehyde, then stained with DAPI (D9542-1MG, Sigma), CellMask (C10045, ThermoFisher), and Phalloidin (A22287, ThermoFisher). Images were taken using a ZEISS LSM 900 confocal microscope with Airyscan 2. The length of individual sprouts was measured from the spheroid margin to the sprout apex using ImageJ (NIH).

#### RNA extraction, reverse transcription, and real-time PCR

Total RNA was isolated from cells using the MiniBEST Universal RNA Extraction Kit (TaKaRa) and reverse-transcribed to cDNA with the First-Strand cDNA Synthesis SuperMix (TransGen Biotech). RT–qPCR was performed using TB Green Premix Ex Taq (TaKaRa) on the 7500 Real-Time PCR system (Applied Biosystems). Primers sequences used in this study were as follows: *Ddi2*, F: 5′-GTGATGTTGTGATTCTAC-3′, R: 5′-TATGCTACTGAAGTCAAT-3′; *β-Actin*, F: 5′-GGCTGTATTCCCCTCCATCG-3′, R: 5′-CCAGTTGGTAACAATGCCATGT-3′.

#### Zebrafish husbandry

Transgenic fishline *Tg(flk:GFP)* was maintained under standard conditions (Westerfield, 1995). Embryos from natural spawning were collected in E3 medium (5 mM NaCl, 0.17 mM KCl, 0.33 mM $CaCl_2$, and 0.33 mM $MgSO_4$, pH 7.2) in Petri dishes and the medium was replaced twice daily. Embryos over 24 hpf were treated with 0.003% PTU (1-phenyl-2-thiourea, Sigma, P7629) to prevent pigmentation for observing vascular phenotypes. All experiments were performed according to institutional and national ethical and animal welfare guidelines.

#### Morpholinos and mRNA injection

The following MOs (Gene Tools, LLC) were injected into one-cell stage embryos as described (Yuan & Sun, 2009). *amot*-MO, 5′-CCTTACTTGACCTATTGAGGAGCAG-3′ (Aase *et al*, 2007); *lpa1*-MO, 5′-TGGAGCACTTACCCAATACAATCAC-3′ (Lee *et al*, 2008; Yukiura *et al*, 2011); *lpa4*-MO, 5′-GGCCATTTTGGCACTTGCAGTAGAT-3′ (Yukiura *et al*, 2011); *tnksa*-MO, 5′-ACGTCGCCATTTTCGCACACAAATC-3′ (Wang *et al*, 2015a); *tnksb*-MO, 5′-GTGAGGATCGACGGGACACCGCCAT-3′ (Wang *et al*, 2015a); *rnf146*-MO, 5′-CTAGCCATACTGACAATGTAGCCGA-3′; *ddi2*-MO, 5′-CTTCTCTCTCGCTGTCAGAAACT-3′. cDNA sequences of human AMOTp130, AMOT-CT, AMOT-NT, AMOT-ΔTBD, and AMOT-Δcut were inserted into pcDNA3.1 vector. mRNAs were then synthesized by *in vitro* transcription using the mMESSAGE mMACHINE kit (Ambion) and purified by MEGAclear kit (Invitrogen) according to the manufacturer's instructions. Injection dosage was as follows: 8 ng *amot*-MO; 7.6 ng *lpa1*-MO + 3.8 ng *lpa4*-MO; 6.4 ng *tnksa*-MO + 6.4 ng *tnksb*-MO; 20.8 ng *rnf146*-MO; 9.6 ng *ddi2*-MO; 8 ng *amot*-MO + 440 pg *hAMOTp130*; 8 ng *amot*-MO + 400 pg *hAMOT-CT*; 8 ng *amot*-MO + 120 pg *hAMOT-NT*; 8 ng *amot*-MO + 440 pg *hAMOT-ΔTBD*; 8 ng *amot*-MO + 440 pg *hAMOT-Δcut*; 9.6 ng *ddi2* 2-MO + 440 pg *hAMOTp130*; 9.6 ng *ddi2*-MO + 400 pg *hAMOT-CT*.

#### Zebrafish imaging

Zebrafish embryos were embedded in 1% low melting agarose for imaging. Fluorescent images were obtained using a Zeiss Axio Observer.Z1-inverted microscope equipped with an Apotome, and 3D projections were generated by Zeiss Zen software.

#### Mouse models

The Animal Ethics Committee of Shanghai Medical College, Fudan University approved all mouse experiments. Transgenic *Nf2*$^{fl/fl}$ mouse was generated as described in the previously published paper (Wang *et al*, 2021). *AMOT-Δcut* KI (Amot-e(c.394-399del)1), *AMOT-CT* (R26-e(CAG-LSL-mNeoGreen-FLAG-AMOT-132–1084aa)), *AMOT-Δcut* (R26-e(CAG-LSL-mNeoGreen-FLAG-AMOT-Δ131132aa)), and *Ddi2*$^{fl/fl}$ mice were in-house generated as described in Appendix Figs S4–S6 and S9. *Cdh5-(PAC)-cre*ERT2 mice are used to delete or overexpress genes in endothelial cells (Zhao *et al*, 2019). The detailed information about the mouse strains is shown in Table 1. In order to induce gene deletion, P3-P5 or P1-P3 pups received three consecutive intraperitoneal injections with 50 μl tamoxifen (Sigma, T5648; 2 mg/ml), and the retinas were collected at P5 to P7, for further analysis.

#### Retina dissection and staining

Mice were sacrificed and eyes were fixed in 4% paraformaldehyde for 90 min on ice. The retinas were dissected out, washed in PBS, and blocked for 2 h at RT in blocking buffer (0.5% block reagent (FP1012, PerkinElmer) in TNT buffer). Next, the retinas were incubated in blocking buffer with diluted primary antibody (anti-ERG, 1:200, ab92513, Abcam) and Alexa-Fluor-conjugated Isolectin B4 (121411 or 121412, 20 μg/ml, Invitrogen) overnight at 4°C. The retinas were washed three times (30 min each time) in TNT buffer (150 mM NaCl, 100 mM Tris–HCl (pH 7.4), 0.4% Triton X-100 in $H_2O$) and then incubated with Alexa-Fluor 488/555/647 conjugated secondary antibodies (1:200, Invitrogen) for 2 h. After washing and flat-mounting (Fluromount-G, Invitrogen), retinas were analyzed using a confocal fluorescence microscope (Leica SP8 and Zeiss LSM900). Quantification was done with ImageJ (NIH).

#### Retina analysis and quantification

Retina analysis and quantification were performed according to the published protocol (Pitulescu *et al*, 2010). Briefly, EC coverage was calculated by normalizing IB4-positive area to total retinal area using images of the whole retina. For the quantification of sprout number and length, we defined the angiogenic front as the line connecting the bases of sprouting ECs and counted the number and

length of sprouts along the angiogenic front. The ratio of sprout number in each field per 100-μm endothelial vessel length and the mean length of sprouts were calculated. Number of nuclei was counted along the sprouting front border per 100-μm endothelial vessel length. Branch points were defined as junctions of capillary segments and counted using vascular plexus images taken between an artery and a vein. In the oxygen-induced retinopathy model, the avascular area was defined as the ratio of central avascular area and whole retinal area, and the sprouting area was quantified in the red stippled area. Image analysis and quantification were performed with ImageJ (NIH) and Adobe Photoshop.

#### Oxygen-induced retinopathy model

OIR was performed as described in the published protocol (Connor *et al*, 2009). In brief, P7 pups and breeding mothers were exposed to 75% $O_2$ until P12. In this process, two breeding mothers were used for rotation every other day. Then, the pups were exposed to room air until P15 ($CT^{iEC\text{-}TG}$ mice) or P17(*Δcut* KI mice). Eyes were collected and retinas were stained with IB4 and ERG antibody, and avascular and sprouting areas were measured.

#### Quantification and statistical analysis

Statistical analyses were performed using GraphPad Prism 9 software (GraphPad Software, Inc., USA). All representative experiments shown were repeated three or more times as reported in the figures and corresponding figure legends. The results were expressed as the mean ± SEM. Statistical significance was determined using the Student's *t*-test between groups. $*P < 0.05$, $**P < 0.01$, $***P < 0.001$, n.s. indicates not significant.

## Data availability

This study includes no data deposited in external repositories.

**Expanded View** for this article is available online.

### Acknowledgements
We would like to thank Drs. Junhao Hu, Zhengjun Chen, and Xiaohong Wang for technical help and comments. This study is supported by grants from the National Key R&D program of China (2018YFA0800304, 2020YFA0803202), National Natural Science Foundation of China (32200570, 32170852), Science and Technology Commission of Shanghai Municipality (19JC1411100, 21S11905000), Shanghai Municipal Health Commission (2022XD049), and China Postdoctoral Science Foundation (2022TQ0076, 2022M710788). This work is also supported by the Medical Science Data Center in Shanghai Medical College of Fudan Univeristy.

### Author contributions
**Ruilin Zhang:** Conceptualization; writing – original draft. **Fa-Xing Yu:** Conceptualization; supervision; funding acquisition; writing – original draft; writing – review and editing. **Yu Wang:** Conceptualization; data curation; formal analysis; writing – original draft; writing – review and editing. **Yuwen Zhu:** Data curation; formal analysis; writing – original draft; writing – review and editing. **Yebin Wang:** Formal analysis. **Yue Chang:** Data curation. **Fang Geng:** Data curation. **Mingyue Ma:** Data curation. **Yuan Gu:** Data curation. **Aijuan Yu:** Data curation. **Pengcheng Yu:** Data curation. **Zhao Sha:** Data curation. **Sixian Qi:** Data curation. **Jian Li:** Data curation. **Wencao Zhao:** Data curation. **Rui Zhu:** Data curation. **Weijun Pan:** Resources.

### Disclosure and competing interests statement
The authors declare that they have no conflict of interest.

## References

Aase K, Ernkvist M, Ebarasi L, Jakobsson L, Majumdar A, Yi C, Birot O, Ming Y, Kvanta A, Edholm D *et al* (2007) Angiomotin regulates endothelial cell migration during embryonic angiogenesis. *Genes Dev* 21: 2055 – 2068

Adams RH, Alitalo K (2007) Molecular regulation of angiogenesis and lymphangiogenesis. *Nat Rev Mol Cell Biol* 8: 464 – 478

Adler JJ, Heller BL, Bringman LR, Ranahan WP, Cocklin RR, Goebl MG, Oh M, Lim HS, Ingham RJ, Wells CD (2013a) Amot130 adapts atrophin-1 interacting protein 4 to inhibit yes-associated protein signaling and cell growth. *J Biol Chem* 288: 15181 – 15193

Adler JJ, Johnson DE, Heller BL, Bringman LR, Ranahan WP, Conwell MD, Sun Y, Hudmon A, Wells CD (2013b) Serum deprivation inhibits the transcriptional co-activator YAP and cell growth via phosphorylation of the 130-kDa isoform of Angiomotin by the LATS1/2 protein kinases. *Proc Natl Acad Sci USA* 110: 17368 – 17373

Apte RS, Chen DS, Ferrara N (2019) VEGF in signaling and disease: beyond discovery and development. *Cell* 176: 1248 – 1264

Benhamouche S, Curto M, Saotome I, Gladden AB, Liu CH, Giovannini M, McClatchey AI (2010) Nf2/Merlin controls progenitor homeostasis and tumorigenesis in the liver. *Genes Dev* 24: 1718 – 1730

Campbell CI, Samavarchi-Tehrani P, Barrios-Rodiles M, Datti A, Gingras AC, Wrana JL (2016) The RNF146 and tankyrase pathway maintains the junctional crumbs complex through regulation of angiomotin. *J Cell Sci* 129: 3396 – 3411

Carmeliet P (2003) Angiogenesis in health and disease. *Nat Med* 9: 653 – 660

Chan SW, Lim CJ, Chong YF, Pobbati AV, Huang C, Hong W (2011) Hippo pathway-independent restriction of TAZ and YAP by angiomotin. *J Biol Chem* 286: 7018 – 7026

Chan SW, Lim CJ, Guo F, Tan I, Leung T, Hong W (2013) Actin-binding and cell proliferation activities of angiomotin family members are regulated by hippo pathway-mediated phosphorylation. *J Biol Chem* 288: 37296 – 37307

Connor KM, Krah NM, Dennison RJ, Aderman CM, Chen J, Guerin KI, Sapieha P, Stahl A, Willett KL, Smith LE (2009) Quantification of oxygen-induced retinopathy in the mouse: a model of vessel loss, vessel regrowth and pathological angiogenesis. *Nat Protoc* 4: 1565 – 1573

Dai X, She P, Chi F, Feng Y, Liu H, Jin D, Zhao Y, Guo X, Jiang D, Guan KL *et al* (2013) Phosphorylation of angiomotin by Lats1/2 kinases inhibits F-Actin binding, cell migration, and angiogenesis. *J Biol Chem* 288: 34041 – 34051

Ernkvist M, Luna Persson N, Audebert S, Lecine P, Sinha I, Liu M, Schlueter M, Horowitz A, Aase K, Weide T *et al* (2009) The Amot/Patj/Syx signaling complex spatially controls RhoA GTPase activity in migrating endothelial cells. *Blood* 113: 244 – 253

Gu Y, Wang X, Wang Y, Wang Y, Li J, Yu FX (2020) Nelfinavir inhibits human DDI2 and potentiates cytotoxicity of proteasome inhibitors. *Cell Signal* 75: 109775

Hamaratoglu F, Willecke M, Kango-Singh M, Nolo R, Hyun E, Tao C, Jafar-Nejad H, Halder G (2006) The tumour-suppressor genes NF2/Merlin and Expanded act through hippo signalling to regulate cell proliferation and apoptosis. *Nat Cell Biol* 8: 27 – 36

 

He J, Bao Q, Zhang Y, Liu M, Lv H, Liu Y, Yao L, Li B, Zhang C, He S *et al* (2018) Yes-associated protein promotes angiogenesis via signal transducer and activator of transcription 3 in endothelial cells. *Circ Res* 122: 591 – 605

Hultin S, Zheng Y, Mojallal M, Vertuani S, Gentili C, Balland M, Milloud R, Belting HG, Affolter M, Helker CS *et al* (2014) AmotL2 Links VE-cadherin to contractile Actin fibres necessary for aortic lumen expansion. *Nat Commun* 5: 3743

Ishii I, Fukushima N, Ye X, Chun J (2004) Lysophospholipid receptors: signaling and biology. *Annu Rev Biochem* 73: 321 – 354

Kim J, Kim YH, Kim J, Park DY, Bae H, Lee DH, Kim KH, Hong SP, Jang SP, Kubota Y *et al* (2017) YAP/TAZ regulates sprouting angiogenesis and vascular barrier maturation. *J Clin Invest* 127: 3441 – 3461

Koizumi S, Irie T, Hirayama S, Sakurai Y, Yashiroda H, Naguro I, Ichijo H, Hamazaki J, Murata S (2016) The aspartyl protease DDI2 activates Nrf1 to compensate for proteasome dysfunction. *Elife* 5: e18357

Krock BL, Skuli N, Simon MC (2011) Hypoxia-induced angiogenesis: good and evil. *Genes Cancer* 2: 1117 – 1133

Lee SJ, Chan TH, Chen TC, Liao BK, Hwang PP, Lee H (2008) LPA1 is essential for lymphatic vessel development in zebrafish. *FASEB J* 22: 3706 – 3715

Lehrbach NJ, Ruvkun G (2016) Proteasome dysfunction triggers activation of SKN-1A/Nrf1 by the aspartic protease DDI-1. *Elife* 5: e17721

Lim R, Sugino T, Nolte H, Andrade J, Zimmermann B, Shi C, Doddaballapur A, Ong YT, Wilhelm K, Fasse JWD *et al* (2019) Deubiquitinase USP10 regulates notch signaling in the endothelium. *Science* 364: 188 – 193

Mana-Capelli S, Paramasivam M, Dutta S, McCollum D (2014) Angiomotins link F-Actin architecture to hippo pathway signaling. *Mol Biol Cell* 25: 1676 – 1685

Mayor R, Etienne-Manneville S (2016) The front and rear of collective cell migration. *Nat Rev Mol Cell Biol* 17: 97 – 109

Meng Z, Moroishi T, Mottier-Pavie V, Plouffe SW, Hansen CG, Hong AW, Park HW, Mo JS, Lu W, Lu S *et al* (2015) MAP4K family kinases act in parallel to MST1/2 to activate LATS1/2 in the hippo pathway. *Nat Commun* 6: 8357

Mercenne G, Alam SL, Arii J, Lalonde MS, Sundquist WI (2015) Angiomotin functions in HIV-1 assembly and budding. *Elife* 4: e03778

Mills GB, Moolenaar WH (2003) The emerging role of lysophosphatidic acid in cancer. *Nat Rev Cancer* 3: 582 – 591

Moleirinho S, Guerrant W, Kissil JL (2014) The Angiomotins – from discovery to function. *FEBS Lett* 588: 2693 – 2703

Paramasivam M, Sarkeshik A, Yates JR 3rd, Fernandes MJ, McCollum D (2011) Angiomotin family proteins are novel activators of the LATS2 kinase tumor suppressor. *Mol Biol Cell* 22: 3725 – 3733

Pitulescu ME, Schmidt I, Benedito R, Adams RH (2010) Inducible gene targeting in the neonatal vasculature and analysis of retinal angiogenesis in mice. *Nat Protoc* 5: 1518 – 1534

Plouffe SW, Meng Z, Lin KC, Lin B, Hong AW, Chun JV, Guan KL (2016) Characterization of hippo pathway components by gene inactivation. *Mol Cell* 64: 993 – 1008

Potente M, Carmeliet P (2017) The link between angiogenesis and endothelial metabolism. *Annu Rev Physiol* 79: 43 – 66

Puente XS, Sanchez LM, Overall CM, Lopez-Otin C (2003) Human and mouse proteases: a comparative genomic approach. *Nat Rev Genet* 4: 544 – 558

Pugh CW, Ratcliffe PJ (2003) Regulation of angiogenesis by hypoxia: role of the HIF system. *Nat Med* 9: 677 – 684

Qi S, Zhu Y, Liu X, Li P, Wang Y, Zeng Y, Yu A, Wang Y, Sha Z, Zhong Z *et al* (2022) WWC proteins mediate LATS1/2 activation by hippo kinases and imply a tumor suppression strategy. *Mol Cell* 82: 1850 – 1864

Rorth P (2012) Fellow travellers: emergent properties of collective cell migration. *EMBO Rep* 13: 984 – 991

Sakabe M, Fan J, Odaka Y, Liu N, Hassan A, Duan X, Stump P, Byerly L, Donaldson M, Hao J *et al* (2017) YAP/TAZ-CDC42 signaling regulates vascular tip cell migration. *Proc Natl Acad Sci USA* 114: 10918 – 10923

Shibuya M (2011) Vascular endothelial growth factor (VEGF) and its receptor (VEGFR) signaling in angiogenesis: a crucial target for anti- and pro-angiogenic therapies. *Genes Cancer* 2: 1097 – 1105

Shimono A, Behringer RR (2003) Angiomotin regulates visceral endoderm movements during mouse embryogenesis. *Curr Biol* 13: 613 – 617

Stahl A, Connor KM, Sapieha P, Chen J, Dennison RJ, Krah NM, Seaward MR, Willett KL, Aderman CM, Guerin KI *et al* (2010) The mouse retina as an angiogenesis model. *Invest Ophthalmol Vis Sci* 51: 2813 – 2826

Sumida H, Noguchi K, Kihara Y, Abe M, Yanagida K, Hamano F, Sato S, Tamaki K, Morishita Y, Kano MR *et al* (2010) LPA4 regulates blood and lymphatic vessel formation during mouse embryogenesis. *Blood* 116: 5060 – 5070

Tetzlaff F, Fischer A (2018) Human endothelial cell spheroid-based sprouting angiogenesis assay in collagen. *Bio Protoc* 8: e2995

Tetzlaff MT, Yu W, Li M, Zhang P, Finegold M, Mahon K, Harper JW, Schwartz RJ, Elledge SJ (2004) Defective cardiovascular development and elevated cyclin E and notch proteins in mice lacking the Fbw7 F-box protein. *Proc Natl Acad Sci USA* 101: 3338 – 3345

Troilo A, Benson EK, Esposito D, Garibsingh RA, Reddy EP, Mungamuri SK, Aaronson SA (2016) Angiomotin stabilization by tankyrase inhibitors antagonizes constitutive TEAD-dependent transcription and proliferation of human tumor cells with hippo pathway core component mutations. *Oncotarget* 7: 28765 – 28782

Tsunematsu R, Nakayama K, Oike Y, Nishiyama M, Ishida N, Hatakeyama S, Bessho Y, Kageyama R, Suda T, Nakayama KI (2004) Mouse Fbw7/Sel-10/Cdc4 is required for notch degradation during vascular development. *J Biol Chem* 279: 9417 – 9423

van Meeteren LA, Ruurs P, Stortelers C, Bouwman P, van Rooijen MA, Pradere JP, Pettit TR, Wakelam MJ, Saulnier-Blache JS, Mummery CL *et al* (2006) Autotaxin, a secreted lysophospholipase D, is essential for blood vessel formation during development. *Mol Cell Biol* 26: 5015 – 5022

Wang W, Huang J, Chen J (2011) Angiomotin-like proteins associate with and negatively regulate YAP1. *J Biol Chem* 286: 4364 – 4370

Wang C, An J, Zhang P, Xu C, Gao K, Wu D, Wang D, Yu H, Liu JO, Yu L (2012) The Nedd4-like ubiquitin E3 ligases target angiomotin/p130 to ubiquitin-dependent degradation. *Biochem J* 444: 279 – 289

Wang H, Semenova S, Kuusela S, Panula P, Lehtonen S (2015a) Tankyrases regulate glucoregulatory mechanisms and somatic growth via the central melanocortin system in zebrafish larvae. *FASEB J* 29: 4435 – 4448

Wang W, Li N, Li X, Tran MK, Han X, Chen J (2015b) Tankyrase inhibitors target YAP by stabilizing Angiomotin family proteins. *Cell Rep* 13: 524 – 532

Wang H, Lu B, Castillo J, Zhang Y, Yang Z, McAllister G, Lindeman A, Reece-Hoyes J, Tallarico J, Russ C *et al* (2016) Tankyrase inhibitor sensitizes lung cancer cells to endothelial growth factor receptor (EGFR) inhibition via stabilizing Angiomotins and inhibiting YAP signaling. *J Biol Chem* 291: 15256 – 15266

Wang X, Freire Valls A, Schermann G, Shen Y, Moya IM, Castro L, Urban S, Solecki GM, Winkler F, Riedemann L *et al* (2017) YAP/TAZ orchestrate VEGF signaling during developmental angiogenesis. *Dev Cell* 42: 462 – 478

Wang Y, Zhu Y, Gu Y, Ma M, Wang Y, Qi S, Zeng Y, Zhu R, Wang X, Yu P *et al* (2021) Stabilization of Motin family proteins in NF2-deficient cells prevents full activation of YAP/TAZ and rapid tumorigenesis. *Cell Rep* 36: 109596

Wells CD, Fawcett JP, Traweger A, Yamanaka Y, Goudreault M, Elder K, Kulkarni S, Gish G, Virag C, Lim C *et al* (2006) A Rich1/Amot complex regulates the Cdc42 GTPase and apical-polarity proteins in epithelial cells. *Cell* 125: 535 – 548

Westerfield M (1995) *The zebrafish book: a guide for the laboratory use of zebrafish (Brachydanio rerio)*. Eugene, OR: University of Oregon Press

Yu FX, Zhao B, Panupinthu N, Jewell JL, Lian I, Wang LH, Zhao J, Yuan H, Tumaneng K, Li H *et al* (2012) Regulation of the hippo-YAP pathway by G-protein-coupled receptor signaling. *Cell* 150: 780 – 791

Yuan S, Sun Z (2009) Microinjection of mRNA and morpholino antisense oligonucleotides in zebrafish embryos. *J Vis Exp* 1113

Yukiura H, Hama K, Nakanaga K, Tanaka M, Asaoka Y, Okudaira S, Arima N, Inoue A, Hashimoto T, Arai H *et al* (2011) Autotaxin regulates vascular development via multiple lysophosphatidic acid (LPA) receptors in zebrafish. *J Biol Chem* 286: 43972 – 43983

Zanconato F, Cordenonsi M, Piccolo S (2016) YAP/TAZ at the roots of cancer. *Cancer Cell* 29: 783 – 803

Zhang N, Bai H, David KK, Dong J, Zheng Y, Cai J, Giovannini M, Liu P, Anders RA, Pan D (2010) The Merlin/NF2 tumor suppressor functions through the YAP oncoprotein to regulate tissue homeostasis in mammals. *Dev Cell* 19: 27 – 38

Zhang Y, Zhang Y, Kameishi S, Barutello G, Zheng Y, Tobin NP, Nicosia J, Hennig K, Chiu DK, Balland M *et al* (2021) The Amot/integrin protein complex transmits mechanical forces required for vascular expansion. *Cell Rep* 36: 109616

Zhao B, Li L, Lu Q, Wang LH, Liu CY, Lei Q, Guan KL (2011) Angiomotin is a novel hippo pathway component that inhibits YAP oncoprotein. *Genes Dev* 25: 51 – 63

Zhao W, Cao L, Ying H, Zhang W, Li D, Zhu X, Xue W, Wu S, Cao M, Fu C *et al* (2019) Endothelial CDS2 deficiency causes VEGFA-mediated vascular regression and tumor inhibition. *Cell Res* 29: 895 – 910

Zheng Y, Vertuani S, Nystrom S, Audebert S, Meijer I, Tegnebratt T, Borg JP, Uhlen P, Majumdar A, Holmgren L (2009) Angiomotin-like protein 1 controls endothelial polarity and junction stability during sprouting angiogenesis. *Circ Res* 105: 260 – 270

 